Title: m^{6}A-mediated epi-transcriptomic dysregulation underlies synaptic dysfunction in fragile X syndrome

Lu Lu[1,2]*, Avijite Kumer Sarkar[1,2]*, Lan Dao[1,2], Yanchen Liu[3], Chunlong Ma[4], Phyo Han Thwin[4], Xuyao Chang[1,2], George Yoshida[1,2], Annie Li[1], Cenjing Wang[1], Crace Westerkamp[3], Lauren Schmitt[3], Maag Chelsey[5], Monzon Stephanie[5], Yu Zhao[6], Yaping Liu[5], Xiong Wang[7], Ling-Qiang Zhu[8], Dan Liu[8], Jason Tchieu[1,2], Makoto Miyakoshi[3], Haining Zhu[4], Christina Gross[9], Ernest Pedapati[3], Nathan Salomonis[10], Craig Erickson[3], Ziyuan Guo[1,2#]

1. Center for Stem Cell and Organoid Medicine (CuSTOM), Division of Developmental Biology, Cincinnati Children's Hospital Medical Center, Cincinnati, OH 45229, USA;
2. Department of Pediatrics, University of Cincinnati, College of Medicine, Cincinnati, OH 45229, USA;
3. Division of Child and Adolescent Psychiatry, Cincinnati Children's Hospital Medical Center, Cincinnati, OH 45229, USA;
4. Department of Pharmacology and Toxicology, R. Ken Coit College of Pharmacy, University of Arizona, AZ 85721, USA;
5. Division of Human Genetics, Cincinnati Children's Hospital Medical Center, Cincinnati, OH 45229, USA;
6. Department of Computer Science, University of Cincinnati, Cincinnati, OH 45221, USA.
7. Department of Laboratory Medicine, Tongji Hospital, Tongji Medical College, Huazhong University of Science and Technology, Wuhan, China;
8. Department of Pathophysiology, Key Lab of Neurological Disorder of Education Ministry, School of Basic Medicine, Tongji Medical College, Huazhong University of Science and Technology, Wuhan, Hubei, China;
9. Division of Neurology, Cincinnati Children's Hospital Medical Center, Cincinnati, OH 45229, USA;
10. Division of Biomedical Informatics, Cincinnati Children's Hospital Medical Center, Cincinnati, OH 45229, USA.

*These authors contributed equally to this work

Correspondence should be addressed to Ziyuan Guo (Ziyuan.Guo@cchmc.org)

33 Leading contact: Ziyuan Guo, Division of Developmental Biology, Department of Pediatrics,
34 Cincinnati Children's Hospital Medical Center, 3333 Burnet Avenue, Cincinnati, OH 45229, USA.
35 Tel: 513-517-7092, Email: Ziyuan.Guo@cchmc.org.
36
37 **Declaration of interests:** The authors have declared no conflicts of interest.

Abstract

Fragile X syndrome (FXS), the leading genetic cause of intellectual disability, arises from *FMR1* gene silencing and loss of the FMRP protein. FMRP is known to bind to and regulate the stability of m^6A-containing transcripts. However, how loss of FMRP impacts on transcriptome-wide m^6A modifications in FXS patients remains unknown. To answer this question, we generated cortical neurons differentiated from induced pluripotent stem cells (iPSC) derived from healthy subjects and FXS patients. In electrophysiology recordings, we validated that synaptic and neuronal network defects in iPSC-derived FXS neurons corresponded to the clinical EEG data of the patients from which the corresponding iPSC line was derived. In analysis of transcriptome-wide methylation, we show that FMRP deficiency led to increased translation of m^6A writers, resulting in hypermethylation that primarily affecting synapse-associated transcripts and increased mRNA decay. Conversely, in the presence of an m^6A writer inhibitor, synaptic defects in FXS neurons were rescued. Taken together, our findings uncover that an FMRP-dependent epi-transcriptomic mechanism contributes to FXS pathogenesis by disrupting m^6A modifications in FXS, suggesting a promising avenue for m^6A-targeted therapies.

Introduction

Fragile X syndrome (FXS) is the most common inherited cause of intellectual disability, and as it often co-occurs with autism spectrum disorders (ASD), is believed to make genetic contributions to both. The syndrome manifests as a spectrum of cognitive impairments and socio-emotional deficits. FXS is primarily caused by the presence of expanded trinucleotide repeats in the fragile X messenger ribonucleoprotein 1 (*FMR1*) gene, leading to transcriptional silencing and consequent loss of Fragile X mental retardation protein (FMRP). With excessive glutamatergic signaling a pathological hallmark of FXS, previous research primarily focused on excitatory synaptic transmission, and in particular signaling downstream of the metabotropic glutamate receptor subtype 5 (mGluR5) [1, 2]. However, given the limited success of mGluR5-targeted therapies, the focus has shifted towards assessing how the balance between excitatory and inhibitory (E/I) signaling impact on network hyperexcitability [3-6]. Despite insights gained from FMRP loss-of-function studies in animal models, clinical trials for FXS, while showing promise in preclinical studies, have yielded limited success [7, 8]. More recently, advancements have been made in modeling FXS using patient-derived induced pluripotent stem cells (iPSCs) [9-14], which mirror neurodevelopmental and synaptic abnormalities within the human cellular and genetic context. However, the extent to which human cultured neurons faithfully recapitulate FXS-associated disease phenotypes *in vitro* and in a way that could inform development of

therapeutic strategies remains uncertain. Consequently, bridging the gap between experimental models and human disease holds paramount importance in advancing FXS research.

N6-methyladenosine (m^6A) is a prevalent RNA modification in mammalian messenger RNAs (mRNAs). It is installed by 'writers' (known as methyltransferases) like the METTL3/14 complex, including METTL3, METTL14, and WTAP[15-20], and removed by 'erasers' such as Fat Mass and Obesity-Associated Protein (FTO) and AlkB Homolog 5 (ALKBH5) [20-22]. The m^6A modification instructs regulation of RNA processes such as splicing, export, translation, and decay through the actions of m^6A 'readers' that bind m^6A-marked mRNAs[20, 23-25]. In the nervous system, m^6A modifications are particularly abundant and play established roles in brain development and neuronal functions [26-31]. Genome-wide association studies (GWAS) have identified rare and *de novo* variants of the m^6A reader YTHDC2 [32-35] that are strongly associated with ASD (SFARI Gene Score 2). However, our understanding of m^6A regulation in human neurons, especially under pathological conditions, is still in its infancy. Consequently, transcriptome-wide m^6A profiling in patient-derived neurons stands to significantly advance our understanding of how this modification impacts on pathological events and neuronal dysfunction.

FMRP, a multifunctional RNA-binding protein [36] primarily localized to translating polyribosomes, regulates local protein synthesis at synapses [37-39]. Its deficiency results in increased synthesis of synapse-related proteins. Recently identified as a putative m^6A 'reader' via unbiased proteomics studies [40-42], FMRP influences a range of neural processes such as neural progenitor proliferation and differentiation, synaptic transmission, plasticity, and axon growth [43-47]. Despite a conserved consensus sequence between FMRP-binding sites and m^6A methylation, FMRP interacts directly with m^6A 'readers' in an m^6A-modified mRNA-independent manner [46, 47] and negatively regulates their functions [45-47]. Specifically, FMRP antagonizes the activity of m^6A readers, YTHDF2 and YTHDF1 (as well as the Drosophila homolog ythdf), stabilizing m^6A-marked mRNAs and controlling their translation [45-47]. However, the precise mechanisms by which FMRP deficiency impacts transcriptome-wide m^6A modifications in patient-derived neurons remains elusive, and especially, to what extent this modification impacts on synaptic and neuronal dysfunction, eventually contributing to FXS pathology.

Here, we established a patient-derived iPSC neuron model of FXS and identified an imbalance in excitatory/inhibitory (E/I) signaling that correlated with each individual's clinical electroencephalogram (EEG) data. Notably, loss of FMRP leads to elevated m^6A levels in both

FXS patient-derived neurons and *Fmr1* Knockout mice brains. In mechanistic studies, we uncovered that FMRP deficiency disrupts the translational control of m^6A writer expression, leading to accumulation of excessive m^6A-tagged transcripts related to synapse function in FXS neurons and increased mRNA decay of such synapse-related genes. Conversely, treatment with a m^6A writer inhibitor, capable of reducing excessive m^6A modifications, mitigated synaptic and functional defects in FXS neurons by restoring mRNA stability. Our findings unveil a novel m^6A-mediated epi-transcriptomic mechanism underlying FXS, by which FMRP deficiency leads to increased translation of m^6A writers, resulting in transcriptome-wide hypermethylation and points to potential translational significance of m^6A-modifying drugs as promising therapeutics for FXS treatment.

Result

Modeling FXS using patient-derived iPSCs and cortical neurons

In this study, we enrolled seven individuals with FXS and performed neuropsychological examinations on five of them, documenting significantly lower full-scale intelligence quotient (FSIQ, 45.71 $\pm$ 8, n = 5 FXS subjects), nonverbal IQ (NVIQ, 34.04 $\pm$ 8.95, n = 5 FXS subjects) and verbal IQ (VIQ, 57.38 $\pm$ 8.24, n = 5 FXS subjects), indicative of intellectual disability (Table 1). We also validated that FMRP protein levels and FMR1 mRNA levels in blood samples from FXS patients were low or absent (Table 1).

To model FXS, we generated induced pluripotent stem cells (iPSCs) from these seven FXS patients and age- and gender-matched healthy controls, and confirmed pluripotency, stemness, and karyotype integrity of all the iPSC lines (Table 1). We also confirmed via PCR and Asuragen testing that CGG repeat numbers were elevated in FXS patients (over 200 CGG repeats in the 5' UTR of the FMR1 gene compared with 30 or fewer in healthy controls; Table 1 and Supplemental Figure 1a). The expression of forebrain cortical neural progenitor markers (Sox2, Nestin, ZO1, FOXG1, OTX2, PAX6) and mature neuronal markers (Tuj1, CaMKII), along with cortical layer markers (BRN2, CTIP2, TBR1), indicated successful induction of neuroepithelial cell fate (Figure 1a, b and Supplemental Figure 1b, c). Importantly, the FXS patient-derived cortical neurons lacked FMRP expression, unlike their control counterparts (Figure 1c, d), replicating a hallmark of FXS pathology.

In western blot and immunostaining analysis, we identified elevated levels of synaptic proteins Synapsin II and SV2 (Figure 1e, f) and an increase in numbers of synaptic puncta (Figure 1g, h) in the FXS cortical neurons. We also detected distinct alterations in spine morphology, including reduced mushroom-like spines and increased numbers of filopodia-like

spines compared to control neurons (Figure 1i-k). However, we did not detect any significant differences in neurites including number of sections, total neurite length, terminal points, branch points, maximum section length, minimum section length, and mean section length between FXS neurons and controls (Supplemental Figure 1d-l). Taken together, these observations align with previous research linking the absence of FMRP to changes in synaptic protein expression and synaptic structure in FXS neurons [10, 11, 48-51].

Dysregulated synaptic transmission, excitatory/inhibitory imbalance, and hyperexcitability in cortical neurons derived from FXS iPSCs

To delve into the functional aspects of our iPSC model system, we conducted comprehensive electrophysiological analyses, including whole-cell patch-clamp and micro-electrode arrays (MEA). In whole-cell patch-clamp recordings (Figure 2a), we noted a consistent and significant increase in excitatory synaptic transmission in FXS cortical neurons relative to controls (Figure 2b). Specifically, the inter-event interval was decreased in excitatory postsynaptic currents (EPSC) whereas the frequency was elevated but the amplitude reduced (Figure 2c, d). We also observed an overall decrease in inhibitory synaptic transmission in FXS cortical neurons relative to controls (Figure 2e), manifested as an increase in inter-event interval and lower frequency and amplitudes of inhibitory postsynaptic currents (IPSC) (Figure 2f, g).

Beyond the synaptic transmission defects and E/I imbalance, FXS cortical neurons were hyperexcitable, reflected as an increased frequency of evoked action potentials (APs) and decreased thresholds to firing APs (Figure 2i, j). Other parameters, including evoked AP amplitude and Rheobase, remained unchanged (Supplemental Figure 2a, b). Additionally, the frequency of spontaneous AP was higher in FXS cortical neurons relative to control cortical neurons (Figure 2k, l). However, we did not observe any significant disparities in sodium and potassium channel activities between FXS and control neurons (Supplemental Figure 2c-e). Taken together, our data thus far suggested a causal relationship between E/I imbalance and hyperexcitability in FXS iPSC-derived cortical neurons.

Hyperactivity and hyperconnectivity in cortical circuitry derived from FXS iPSCs

To monitor cortical circuitry activity, we cultured 0.5 million neurons on a MEA chip with 64 electrodes and recorded field potentials for 5 minutes at 4, 5, 6, 7, and 8 weeks (Figure 3a and Supplemental Figure 3a). Data were sampled at 20 kHz with a 1-1000 Hz frequency bandwidth (see Methods). We identified spikes based on a threshold (5.5 times the standard deviation of peak-to-peak noise), and bursts as sequences of at least 3 spikes with inter-spike intervals

174 within 300 milliseconds and a duration exceeding 200 milliseconds. In FXS iPSC-derived
175 cortical circuitry, we found heightened spike and burst activity in sample traces (Figure 3b),
176 characterized by a decreased inter-spike interval, increased burst duration, and more spikes per
177 burst, indicative of hyperactivity (Figure 3c-e).
178 Additionally, analysis of array-wide spike detection rate (ASDR) revealed enhanced
179 neuronal network synchrony and hyperconnectivity in FXS iPSC-derived cortical microcircuitry
180 (Figure 3f), reflected as increased burst peak and duration, more active electrodes per network
181 burst, and elevated spike numbers in network bursts (Figure 3g-j). When sorting spikes for each
182 electrode based on waveforms, we found significantly more waveforms in FXS iPSC-derived
183 cortical microcircuitry (Supplemental Figure 3b, c), indicating more synchronized neurons in
184 FXS cortical circuitry. Lastly, UP-state analysis, associated with synchronized activity across a
185 network of neurons, particularly in the cortex, exhibited longer durations in FXS iPSC-derived
186 cortical circuitry (Figure 3k, l). Taken together, these electrophysiological findings identify both
187 cortical network hyperactivity and hyperconnectivity in the FXS cortical microcircuitry.
188 To bridge the gap between *in vitro* models and patients, we examined
189 electroencephalogram (EEG) recordings from the same individuals and correlated these with
190 clinical neuropsychological symptoms. We had already noted deviations in FSIQ, NVIQ, and
191 VIQ in FXS subjects as indications of intellectual disabilities (Table 1). Additionally, we assessed
192 the absolute neural power spectral densities (PSDs) of typically developing control (TDC) and
193 FXS EEG data (Supplemental Figure 3d). We found high gamma power in FXS subjects (Figure
194 3m), which is associated with hyperactivity and inversely correlated with NVIQ in FXS subjects
195 [52-55]. Using FOOOF (Fitting Oscillations and One-Over-F) analysis to parameterize the PSDs [56,
196 57], we found that the FOOOF slope was higher in FXS subjects (Figure 3n), an additional
197 indication of cortical hyperactivity and hyperconnectivity. Taken together, these findings strongly
198 suggest that key pathophysiological signatures in FXS patients such as cortical hyperactivity
199 and hyperconnectivity can be modeled in patient-derived neurons, underscoring the
200 translational potential and clinical relevance of our human model system in uncovering disease-
201 related mechanisms.
202
203 **FMRP-bound mRNAs encoding m^{6}A writers and FMRP deficiency increasing writer**
204 **expression**
205 Like FMRP, the mRNA modification m^{6}A is highly enriched in the brain, where it plays a crucial
206 role in neurodevelopment and in mature neurons [26-31]. To quantify total m^{6}A levels, we purified
207 mRNAs and conducted dot plot analysis using an anti-m^{6}A antibody to detect m^{6}A tag-tagged

208 mRNAs. Relative to control, m^6A levels were notably increased in FXS iPSC-derived cortical
209 neurons (Figure 4a). Additionally, we found increased protein, but not mRNA, expression of m^6A
210 writers, including METTL3, METTL14, and WTAP, the key METTL3/14 complex components
211 (Figure 4b-d). We documented similar findings in *Fmr1* knockout mice (Supplemental Figure 4).
212 These findings suggest that FMRP deficiency leads to elevated m^6A levels through upregulation
213 of m^6A writer protein expression.
214 To determine whether FMRP binds mRNAs encoding m^6A writers, we transfected HEK293T
215 cells with flag-mCherry-FMRP and flag-mCherry plasmids, and conducted pulldown using anti-
216 flag M2 affinity gel (Figure 4e) [58]. In the pulldowns with flag-tagged mCherry-FMRP, but not with
217 flag-tagged mCherry, we observed significant enrichment of METTL3, METTL14, and WTAP
218 mRNAs (Figure 4f). There was no specific enrichment for GAPDH mRNAs, indicating that FMRP
219 binds METTL3, METTL14, and WTAP mRNAs. To investigate whether FMRP regulates
220 translation of the m^6A writer translation, we analyzed the translationally active heavy polysome
221 fractions (see Methods)[59]. Indeed, in FXS patient-derived neurons, METTL3, METTL14, and
222 WTAP were all significantly enriched in the heavy polysome fraction (Figure 4g). In addition, the
223 overall protein translation efficiency increased by 23.5% in FXS neurons (Figure 4h). These
224 findings suggest that basal translation of m^6A writer mRNAs is enhanced in the absence of FMRP.
225
226 **Transcriptome-wide m^6A dysregulation in cortical neurons derived from FXS iPSCs**
227 As a comprehensive profiling of transcriptome-wide m^6A modifications in the context of FXS
228 remains outstanding, we next performed methylated RNA immunoprecipitation sequencing
229 (MeRIP-Seq) of neurons derived from six FXS patients and seven control samples (see
230 Methods). When comparing datasets, we identified 3,313 m^6A-enriched genes in FXS patient-
231 derived neurons and 2,815 enriched genes in controls, with a widespread distribution across all
232 chromosomes (Figure 5a). This data set indicates a transcriptome-wide neuronal dysregulation
233 of m^6A modifications in patients with FXS. Motif analysis and the distribution of m^6A peaks
234 confirmed the robustness of MeRIP-Seq and m^6A analysis, with a predominant GGAC motif
235 near the stop codon (Figure 5b, c). For benchmarking, we conducted MeRIP-Seq on
236 postmortem cortex tissues derived from FXS subjects and healthy controls (Table 2), and
237 validated motif analysis and m^6A peak distributions, (Supplemental Figure 5a-c). Notably, we
238 identified over 9,000 dys-methylated sites between controls and FXS neurons (Figure 5d) and
239 over 4,000 dys-methylated sites between control and FXS postmortem cortex tissues
240 (Supplemental Figure 5d), indicating transcriptome-wide m^6A dysregulation in cultured FXS

241 neurons and in brain tissues. Interestingly, the majority of genes exhibited one hyper- or hypo-
242 methylation site across all chromosomes (Figure 5 e, f and Supplemental Figure 5e, f).
243 When we conducted gene ontology (GO) analysis, we identified significant enrichment of
244 genes with elevated m^6A modifications in categories related to synaptic assembly, structure, and
245 function (Figure 5g and Supplemental Figure 5g). Examples include hypermethylation of genes
246 encoding synaptic proteins, such as SYT3 and SYT5, in exons near the stop codon and 3' UTR
247 (Figure 5h). Notably, genes with elevated m^6A modifications overlapped significantly with
248 previously identified FMRP target genes [38], autism-associated genes from the SFARI database,
249 and synapse-related genes from the SynGO database (Figure 5i-k and Supplemental Figure 5h-
250 j). These data underscore the critical role of excessive m^6A tagging in FXS pathologies,
251 particularly synaptic defects, and its broader implications for autism-spectrum disorders.
252 Furthermore, the prominent overlap between hypermethylated genes and FMRP targets, as well
253 as autism-associated genes, was strongly linked to synapse assembly and function (Figure 5l,
254 m and Supplemental Figure 5k, l), reinforcing that dysregulated m^6A modifications and synaptic
255 dysfunction are central to FXS and autism-spectrum disorders.
256
257 **Dysregulated synapse-related gene expression**
258 We next performed RNA sequencing (RNA-seq) on iPSC-derived neurons from seven healthy
259 controls and six FXS patients (see Methods) and identified over 2,000 significantly differentially
260 expressed genes (DEGs) (Figure 6a). Among these, FMR1 was prominently silenced in FXS
261 iPSC-derived neurons (Figure 6b), consistent with full mutation status (Table 1) and loss of
262 FMRP expression (Figure 1c, d). Through functional enrichment analysis, we identified that
263 nearly all top DEGs categories were linked to synaptic structure and function (Figure 6c).
264 Moreover, DEGs significantly overlapped with FMRP target genes, particularly those associated
265 with synapse-related categories and previously reported synapse-related genes (Supplemental
266 Figure 6a-c). These findings highlight gene expression alterations driving synaptic defects in our
267 iPSC-derived cortical neuron model. Similarly, RNA-seq analysis of cortical postmortem tissues
268 from three FXS patients and healthy controls identified nearly 1,500 significantly altered genes
269 (Supplemental Figure 6d). These genes overlapped with FMRP target and autism-associated
270 genes from the SFARI database (Supplemental Figure 6e-i), highlighting that dysregulated
271 synapse-related gene expression serves as a molecular signature of FXS.
272
273 **Correlation of hypermethylation with gene downregulation and increased mRNA decay**

The regulatory impact of m^6A influences RNA fate and function, modulating various aspects of RNA biology [23-25]. However, whether aberrant m^6A modifications are directly linked to gene expression changes in FXS neurons remains unclear. When we integrated the list of dys-methylated genes (DMGs) (Figure 5) with the DEGs (Figure 6), we revealed a strong correlation between hypermethylation and gene downregulation ("hyper-down" pattern), comprising 64.6% of total correlations ($R = -0.47$, $p < 3.55e-53$, Chi-squared test) (Figure 6d) and indicative of a mechanistic link between hypermethylation and reduced gene expression. Similarly, joint analysis of aberrantly methylated genes and DEGs from FXS postmortem tissues also demonstrated a predominant correlation between hypermethylation and gene downregulation ($R = -0.33$, p-value = 1.152e-53, Chi-squared test), with a notable "hyper-down" pattern in quadrant II (72.9% of total correlations) (Supplemental Figure 6j). These genes were significantly enriched in synapse-related categories (Figure 6e and Supplemental Figure 6k), suggesting that mRNA hypermethylation contributes to synaptic defects by modulating the fate of synapse-related mRNAs, in particular accelerating mRNA decay. Indeed, when we measured mRNA decay rates using actinomycin D treatment and gene-specific RT-qPCR (see Methods), we observed accelerated decay of hypermethylated and downregulated synapse-related transcripts (such as STY7) in FXS neurons (Figure 6f, g). These data suggest that hypermethylation drives transcript degradation and gene downregulation in FXS.

m^6A writer inhibitor rescuing synaptic and functional defects in FXS iPSC-derived cortical neurons

Given the overall increase in m^6A levels (Figure 4a), the association of hypermethylated m^6A marks with downregulated synapse-related genes (Figure 6d), and the observed increase in RNA decay for these hypermethylated genes (Figure 6f), we hypothesized that therapeutic intervention with an m^6A writer inhibitor could alleviate synaptic defects in FXS neurons by restoring normal mRNA stability of synapse-related genes. To test this hypothesis, we treated FXS and control neurons with STM-2457, a small-molecule inhibitor targeting METTL3, the catalytic subunit of the METTL3/14 methyltransferase complex [60]. MeRIP-qPCR (see Methods) revealed that excessive m^6A marks from synapse-related transcripts in FXS neurons were reduced in the presence of STM-2457 but not DMSO (Figure 7a). Additionally, STM-2457 restored the accelerated mRNA decay of synapse-related genes such as LRRC4B in FXS iPSC-derived neurons to control levels (Figure 7b). Notably, the two-week administration of the m^6A writer inhibitor reduced abnormal synaptic puncta and excitatory transmission, while significantly mitigating hyperexcitability in FXS neurons, without affecting normal neuronal function (Figure

7c-h). These findings highlight the critical role of m^6A in FXS synaptic pathology and suggest therapeutic potential of m^6A-modulating drugs in FXS.

Discussion

In this report, we successfully generated iPSC lines from FXS patients matched with controls. We also demonstrated that FXS iPSC-derived neurons recapitulate key aspects of FXS pathology, including *FMR1* gene silencing, loss of FMRP, elevated synaptic protein expression, synaptic puncta, and filopodia-like spines, alongside reduced mushroom spines, consistent with previous related research [48]. Relative to previously reported human PSCs model of FXS [9-13], our system is differentiated by several important features. First, beyond general synaptic transmission defects, our model identified an excitatory/inhibitory imbalance in FXS neurons. Secondly, we characterized a disease-related hyperexcitability and hyperconnectivity in FXS cortical circuitry. Finally, and foremost, these cortical hyperexcitability and hyperconnectivity features were confirmed in the same FXS subjects via analysis of their electroencephalogram (EEG) recording. These findings confirm that cortical hyperexcitability and hyperconnectivity are key pathophysiological signatures in FXS subjects that can be modeled in patient iPSC-derived neuronal models, underscoring the translational potential and clinical relevance of our human model system in uncovering disease-related mechanisms. Taken together, our work represents the first clinically relevant human neuron model for FXS.

In the mammalian brain, m^6A modifications are prevalent mRNA modifications[23-25], known for their roles in brain development and neuronal function [26-30]. Using our human FXS model, we uncovered a disease-associated increase in overall levels of m^6A modifications and validated these findings in *Fmr1* knockout mice. Our mechanistic studies revealed that the increase in m^6A modifications is the result of translational upregulation of m^6A writers—including key components of the METTL3/14 complex, such as METTL3, METTL14, and WTAP—due to FMRP deficiency. These findings provide new insights into how FMRP deficiency contributes to FXS pathology. However, the selective impact of upregulated m^6A writers on synapse-related genes in FXS requires further investigation. Additionally, whether and how FMRP deficiency directly regulates the expression of m^6A erasers and readers awaits future mechanistic studies.

To profile transcriptome-wide m^6A modifications, we conducted MeRIP-Seq on neurons derived from FXS patients and postmortem cortical tissues, comparing them with control samples. We identified several synapse-related genes with hypermethylation sites in both FXS neurons and

342 postmortem tissues, suggesting that m^6A dysregulation contributes to FXS-associated synaptic
343 pathology. Notably, expression of many hypermethylated synapse-related genes was also
344 downregulated, and accompanied by increased mRNA decay, indicating that m^6A-mediated
345 gene regulation involves modulating mRNA stability. In mice, m^6A modifications enhances
346 mRNA decay in neural progenitor cells to regulate normal neurodevelopment. Deficiency in m^6A
347 leads to premature differentiation and neurodevelopmental defects[28]. Additionally, studies in
348 *Fmr1* knockout mice revealed that FMRP's antagonistic interaction with the m^6A reader YTHDF2
349 affects the stability of m^6A-marked target mRNAs [47]. Further mechanistic studies are needed to
350 determine whether YTHDF2 reads m^6A tags on synapse-related transcripts, accelerating their
351 decay in FXS, and whether other m^6A readers (e.g., YTHDF1, YTHDF3, YTHDC1, YTHDC2)
352 modulate other mRNA functions such as alternative splicing and translational efficiency,
353 contributing to FXS pathology.
354
355 In conclusion, our patient-derived iPSC model of FXS mimics clinically relevant cortical
356 hyperexcitability and hyperconnectivity phenotypes. As such, our model bridges the gap
357 between experimental models and human disease and holds paramount importance in
358 advancing FXS research. Specifically, we uncovered a novel m^6A-mediated epi-transcriptomic
359 mechanism underlying FXS, where FMRP deficiency leads to increased translation of m^6A
360 writers, resulting in transcriptome-wide hypermethylation. This hypermethylation, in turn,
361 disrupts the stability of synapse-related transcripts, contributing to FXS pathology. Notably, the
362 m^6A writer inhibitor, capable of reducing excessive m^6A modifications, can retore normal mRNA
363 decay and mitigate disease-related synaptic and neuronal defects in FXS iPSCs-derived
364 neurons. Given the challenges in restoring FMRP function in FXS [36, 61] and the notable genetic
365 implications of the m^6A reader in ASD [32-35], our findings highlight the translational potential of
366 m^6A modifying drug as novel therapeutic treatment for FXS and ASD. In such future directions,
367 we envision that our FXS patient-derived iPSC model could prove useful in discovery or
368 preclinical candidate validation stages of therapeutic development and thereby improve success
369 rates in later-stage clinical trials.

370 **Figure legends**

371 **Figure 1. Synaptic malformations in FXS iPSC-derived cortical neurons. a**. Confocal
372 images of iPSC-derived neurons expressing neuronal markers DCX and TUJ1, cortical layer
373 markers BRN2, CTIP2, and TBR1, and the glutamatergic neuron marker CaMKII. The scale bar
374 is 50 μm. **b**. Quantification of neuronal, cortical layer, and glutamatergic marker expression.
375 Values represent mean ± s.e.m (n = 3 biological repeats per condition). **c-d**. Western blot
376 analysis and quantification of FMRP expression in iPSC-derived cortical neurons from
377 unaffected healthy controls (UHC) and FXS subjects. Values represent mean ± s.e.m. (n = 3 to
378 5 repeats per line; ***p < 0.001, two-tailed t-test). **e-f**. Western blot analysis and quantification of
379 synaptic proteins SV2 and Synapsin II expression in six-week-old UHC and FXS neurons.
380 Values represent mean ± s.e.m. (n = 3 to 5 repeats per line; **p < 0.01, ***p < 0.001, two-tailed
381 t-test). **g-h**. Representative images and quantification of synaptic puncta in six-week-old UHC
382 and FXS neurons stained for the synaptic markers SV2 and Synapsin II. The scale bar is 5 μm.
383 Values represent mean ± s.e.m. (n = 13 to 20 neurons per condition; ***p < 0.001, two-tailed t-
384 test). **i-k**. Illustration of mature and immature spines, confocal images, and quantification
385 showing an increase in the ratio of immature to mature spines in FXS iPSC-derived neurons
386 compared to controls. Arrows point to spines. The scale bar is 5 μm. Values represent mean ±
387 s.e.m. (n = 40 to 45 neurons per condition; ***p < 0.001, two-tailed t-test).

388

389 **Figure 2. Aberrant synaptic transmission, E/I imbalance, and hyperexcitability in FXS**
390 **iPSC-derived cortical neurons. a**. Phase image showing a six-week-old FXS iPSC-derived
391 neuron recorded via patch clamp. The scale bar is 50 μm. **b-d**. Defects in excitatory synaptic
392 transmission in FXS iPSC-derived cortical neurons compared to control neurons. Shown are
393 sample whole-cell voltage-clamp recording traces of excitatory postsynaptic currents (EPSCs)
394 from six-week-old neurons (**b**) and cumulative distribution plots of spontaneous EPSC intervals
395 (**c**, Kolmogorov–Smirnov test, the p-value is approaching zero.) and amplitudes (**d**,
396 Kolmogorov–Smirnov test, p < 2.2e-16). Insets display quantifications of mean frequencies and
397 amplitudes of spontaneous EPSCs. Values represent mean ± s.e.m. (n = 48 to 125 neurons per
398 condition; **p < 0.01, ***p < 0.001, two-tailed t-test). **e-g**. Defects in inhibitory synaptic
399 transmission in FXS iPSC-derived cortical neurons compared to control neurons. Shown are
400 sample whole-cell voltage-clamp traces of spontaneous inhibitory postsynaptic currents (IPSCs)
401 from six-week-old neurons (**e**, V_m = 20 mV), with cumulative distribution plots of spontaneous
402 IPSC intervals (**f**, Kolmogorov–Smirnov test, the p-value is approaching zero.) and amplitudes
403 (**g**, Kolmogorov–Smirnov test, the p-value is approaching zero.). Quantifications of mean

404 frequencies and amplitudes of spontaneous IPSCs are also shown. Values represent mean ±
405 s.e.m. (n = 40 to 58 neurons per condition; ***p < 0.001, two-tailed t-test). **h-l**. Increased
406 excitability in FXS iPSC-derived cortical neurons compared to control neurons. Sample whole-
407 cell current-clamp traces of evoked action potentials (APs) after a 60-pA injection in six-week-
408 old neurons (**h**), with quantifications of evoked AP frequency against injected current (**i**), and
409 threshold (**j**). Sample traces of spontaneous APs (**k**) and quantification of spontaneous AP
410 frequency (**l**) are also provided. Values represent mean ± s.e.m. (n = 45 to 49 neurons per
411 condition; *p < 0.05, **p < 0.01, ***p < 0.001, n.s. denotes non-significant; two-tailed t-test for
412 threshold and spontaneous AP frequency, two-way ANOVA with Tukey's multiple comparisons
413 for evoked AP frequency against injected current).
414
415 **Figure 3. Hyperexcitability and hyperconnectivity conserved between FXS iPSC model**
416 **and the same FXS subject. a**. Schematic illustrating electrophysiological workflows for MEA
417 and EEG recordings in both FXS subjects and their derived neurons. **b-e**. Increased excitability
418 in FXS iPSC-derived cortical neurons compared to control neurons. Shown are sample MEA
419 recording traces of spontaneous spikes from six-week-old neurons (**b**; right panel is an enlarged
420 view of dashed lines in the left panel) and cumulative distribution plots of spontaneous spike
421 intervals (**c**, Kolmogorov–Smirnov test, the p-value is approaching zero.). Quantifications of
422 mean inter-spike interval (Inset), burst duration (**d**), and spikes per burst (**e**) are provided.
423 Values represent mean ± s.e.m. (n = 3 cultures; ***p < 0.001, two-tailed t-test). **f-j**. Enhanced
424 network synchrony and hyperconnectivity in FXS iPSC-derived cortical circuitry compared to
425 controls. **f**. Sample traces and raster plots show array-wide spike detection rate (ASDR) across
426 64 electrodes over 120 seconds. Grey lines indicate network burst detection thresholds, black
427 boxes indicate burst duration, and color codes represent spike frequency. Quantifications of
428 network burst duration (**g**), active electrodes per network burst (**h**), network burst peak (**i**), and
429 spikes per network burst (**j**) are also shown. Values represent mean ± s.e.m. (n = 3 cultures;
430 ***p < 0.001, two-tailed t-test). **k-l**. Prolonged depolarization in FXS iPSC-derived cortical
431 circuitry compared to controls. Shown are sample traces of MEA recording sum amplitude over
432 64 electrodes across 70 seconds in control and FXS cortical circuitry (**k**). Dashed lines indicate
433 thresholds for UP-state detection, with boxes representing UP-state duration. Quantification of
434 UP-state duration is also shown (**l**). Values represent mean ± s.e.m. (n = 3 cultures; ***p <
435 0.001, two-tailed t-test). **m-n**. Cortical hyperactivity and hyperconnectivity in FXS patients.
436 Quantification of absolute power spectral density (PSD) across different frequency bands from
437 EEG data of four typically developing control (TDC) and FXS subjects (**m**). FOOOF (Fitting

438 Oscillations and One-Over-F) plot shows a steeper slope in FXS patients compared to TDC
439 subjects (**n**).
440
441 **Figure 4. FMRP binding to mRNAs encoding m^{6}A writers and the impact of FMRP**
442 **deficiency on writer expression. a**. Elevated m^{6}A levels in FXS iPSC-derived cortical neurons
443 compared to controls. Shown are dot blot assay results for polyA$^+$ RNA m^{6}A levels, with
444 quantification of m^{6}A intensity in FXS iPSC-derived neurons relative to controls, normalized to
445 methylene blue. Values represent mean ± s.e.m. (n = 4 cultures; **p < 0.01; two-tailed t-test). **b**.
446 Transcriptional expression analysis revealing no significant change of METTL3, METTL14, and
447 WTAP transcripts between control and FXS iPSCs-derived neurons. Values represent mean ±
448 s.e.m. (n = 7 control and 6 FXS samples; n.s. denotes non-significant; two-tailed t-test). **c-d**.
449 Western blot analysis and quantification of METTL3, METTL14, and WTAP protein levels.
450 Values represent mean ± s.e.m. (n = 4 cultures; *p < 0.05, **p < 0.01; two-tailed t-test). **e-f**.
451 FMRP binds to mRNAs encoding m^{6}A writers in HEK293T cells. Western blot of flag
452 immunoprecipitation with flag-tagged mCherry–FMRP and flag-tagged mCherry, along with their
453 input samples (**e**). Detection was performed with FMRP and GAPDH antibodies. RT-PCR
454 quantification of GAPDH, METTL3, METTL14, and WTAP mRNA enrichment in pulldown
455 samples (**f**) shows FMRP binding to METTL3, METTL14, and WTAP but not GAPDH mRNAs.
456 Values represent mean ± s.e.m. (n = three biological replicates; ***p < 0.001, n.s. denotes non-
457 significant; two-tailed t-test). **g**. RT-PCR quantification of METTL3, METTL14, and WTAP
458 mRNAs in translationally active heavy polysome fractions from FXS iPSC-derived neurons
459 versus controls. Values represent mean ± s.e.m. (n = 3 biological replicates; *p < 0.05, **p <
460 0.01; two-tailed test). **h**. Polysome profiles demonstrated a profound increase of global
461 translation, as indicated with a 23.5% increase in the ratio of heavy polysomes to monosomes
462 fractions (insert).
463
464 **Figure 5. Transcriptome-wide m^{6}A dysregulation in FXS iPSC-derived cortical neurons. a-**
465 **c**. Transcriptome-wide profiling of m^{6}A in 6-week-old neurons from healthy controls and FXS
466 patients. **a**. Metagene plot showing the distribution of m^{6}A peaks across human chromosomes.
467 **b**. Sequence logo illustrating the top enriched motif in m^{6}A peaks (p-value = 10^{-28}). **c**.
468 Distribution of m^{6}A methylation along transcripts, divided into 5′ UTR, CDS, and 3′ UTR. **d**.
469 Volcano plot depicting MeRIP-seq data for m^{6}A peaks differentially methylated between FXS
470 and control groups (n = 7 healthy controls, 6 FXS samples; adjusted p-value < 0.05; blue and
471 red dots represent significant hypo- and hyper-methylated sites). **e-f**. Histogram showing the

472 distribution of hyper- and hypo-methylated sites per gene (**e**) and per chromosome length
473 across human chromosomes (**f**; blue and red boxes indicate hypo- and hyper-methylated sites).
474 **g**. Gene Ontology (GO) analysis of differentially methylated genes (DMGs) between FXS iPSC-
475 derived neurons and controls, revealing the top 15 enriched cellular component (CC) and
476 biological process (BP) terms. The color represents the adjusted p-value, and the size
477 represents the gene ratio (percentage of DMGs in each GO term). **h**. Integrative Genomics
478 Viewer (IGV) tracks displaying MeRIP-seq read distribution for SYT3 and SYT5 mRNAs. **i-k**.
479 Venn diagrams showing overlap between hypermethylated transcripts and FMRP target
480 transcripts (**i**), SAFRI ASD genes (**j**), and reported synapse-related genes (**k**), along with
481 representation factors and p-values. **l-m**. GO term analysis of genes overlapping between
482 hypermethylated transcripts and FMRP targets (**l**), as well as genes overlapping with SAFRI
483 ASD genes (**m**).
484
485 **Figure 6. Correlation of hypermethylation with gene downregulation and increased mRNA**
486 **decay in synapse-related genes. a**. Volcano plot displaying differential gene expression
487 between FXS iPSC-derived neurons and controls (n = 7 healthy controls, 6 FXS samples; fold
488 change > 1.4, p-value < 0.05; blue and red dots represent significantly down- and up-regulated
489 genes, respectively). **b**. Transcriptional expression analysis revealing significant abundant
490 FMR1 transcripts in control but not FXS iPSCs-derived neurons. Values are shown as mean ±
491 s.e.m. (n = 7 control, 6 FXS samples; *** p < 0.001; two-tailed t-test). **c**. Gene Ontology (GO)
492 term analysis of differentially expressed genes (DEGs) between FXS iPSC-derived neurons and
493 controls, showing the top 15 enrichment terms for cellular component (CC) and molecular
494 function (MF). The color indicates the adjusted P-value, and the size indicates the gene ratio
495 (percentage of total DEGs in each GO term). **d**. Conjoint analysis reveals a strong negative
496 correlation between m^6A modifications and gene expression levels (R = -0.47, p-value = 3.55e-
497 53, Chi-squared test), with a predominant hyper-down pattern in quadrant II (64.6% of total
498 correlations, indicating hyper-methylation paired with gene downregulation). **e**. GO term
499 analysis of hyper-methylated and downregulated transcripts. **f**. mRNA stability assay in FXS
500 iPSC-derived neurons and controls. RNA was isolated at designated time points following
501 actinomycin D treatment, and the stability of STY7 mRNAs was assessed by RT-qPCR (n = 3;
502 *** p < 0.001; two-tailed t-test). **g**. IGV tracks showing MeRIP-seq and RNA-seq read
503 distribution for STY7 mRNAs.
504

505 **Figure 7. Restoration of synaptic and neuronal functions in FXS iPSC-derived cortical**
506 **neurons. a**. MeRIP-qPCR analysis showing relative enrichment of m^6A modifications on
507 synapse-related mRNAs in control and FXS iPSC-derived cortical neurons, with and without
508 STM-2457 treatment. Values represent mean ± s.e.m. (n = 4 biological replicates; *p < 0.05,
509 ***p < 0.001, n.s. denotes non-significant; one-way ANOVA with Tukey's multiple comparisons.).
510 **b**. mRNA stability assay in FXS iPSC-derived neurons and controls, with and without STM-2457
511 treatment. RNA was isolated at specified time points after actinomycin D treatment, and the
512 stability of LRRC4B mRNAs was assessed via RT-qPCR. Values represent mean ± s.e.m. (n =
513 3 biological replicates; ***p < 0.001, n.s. denotes non-significant, one-way ANOVA with Tukey's
514 multiple comparisons.). **c-d**. Representative images and quantification of six-week-old control
515 and FXS neurons, with and without STM-2457 treatment, stained for the synaptic marker
516 Synapsin II. The scale bar is 5 μm. Values represent mean ± s.e.m. (n =10 to 20 neurons per
517 condition; ***p < 0.001, n.s. denotes non-significant; one-way ANOVA with Tukey's multiple
518 comparisons). **e-f**. Sample whole-cell voltage-clamp recordings of excitatory postsynaptic
519 currents (EPSCs) in six-week-old neurons, with and without STM-2457 treatment (**e**), and
520 quantification of mean spontaneous EPSC frequencies (**f**). Values are presented as mean ±
521 s.e.m. (n = 6 to 10 neurons per condition; ***p < 0.001, n.s. denotes non-significant; one-way
522 ANOVA with Tukey's multiple comparisons). **g-h**. Whole-cell current-clamp recordings of evoked
523 action potentials (APs) (**g**), and their quantification (**h**). Values are presented as mean ± s.e.m.
524 (n = 5 to 8 neurons per condition; *p < 0.05, n.s. denotes non-significant; two-way ANOVA with
525 Tukey's multiple comparisons).
526
527
528 **Supplemental Figure legends**
529 **Supplemental Figure 1. Modeling FXS using patient-derived iPSCs. a**. Electropherogram of
530 Asuragen test results showing 29 CGG repeats in UHC-5 and a full mutation with over 200 CGG
531 repeats in FXS-5 iPSC lines. **b**. Confocal images of iPSC-derived neural progenitors expressing
532 markers such as Nestin, Sox2, ZO1, FOXG1, PAX6, and OTX2. The scale bar is 50 μm. **c**.
533 Quantification of neural progenitor marker expression. Values represent mean ± s.e.m. (n = 5 to
534 76 neurons per condition). **d-l**. Semi-automated Sholl analysis reveals no significant differences
535 in neurite parameters between FXS patient-derived cortical neurons and control neurons.
536 Shown are representative images of GFP-labeled FXS and control neurons (**d**), a schematic of
537 neurite analysis (**e**), and quantification of neurite parameters including number of sections (**f**),
538 total neurite length (**g**), terminal points (**h**), branch points (**i**), maximum section length (**j**),

539 minimum section length (**k**), and mean section length (**l**). The scale bar is 50 μm. Values
540 represent mean ± s.e.m. (n = 30 to 169 neurons per condition; n.s. denotes non-significance;
541 two-tailed t-test).
542
543 **Supplemental Figure 2. Sodium and potassium channel activity. a-b**. Quantification of
544 evoked action potential (AP) amplitude (**a**) and rheobase (**b**). Values are presented as mean ±
545 s.e.m. (n = 43 to 92 neurons per condition; n.s. denotes non-significance; two-tailed t-test). **c-e**.
546 Sample whole-cell voltage-clamp recording traces of sodium and potassium channel activity (**c**),
547 along with quantification of sodium (**d**) and potassium (**e**) currents. Values are presented as
548 mean ± s.e.m. (n = 56 to 107 neurons per condition; n.s. denotes non-significance; two-tailed t-
549 test).
550
551 **Supplemental Figure 3. MEA and EEG recordings. a**. Sample bright-field images of human
552 cortical neuron cultures at 6 weeks post-neuronal differentiation. The scale bar is 50 μm. **b-c**.
553 Increased waveforms detected per electrode by automatic spiking sorting in FXS cortical
554 microcircuitry compared to controls. Shown are sample waveforms for electrode 6 and 26 in
555 control and FXS iPSCs-derived cortical microcircuitry (**b**). Quantification of waveforms per
556 channel is also presented (**c**). Values represent mean ± s.e.m. (n = 3 cultures; ***$p < 0.001$; two-
557 tailed t-test). **d**. Power spectral density (PSD) traces across different frequency bands from four
558 typically developing control (TDC) and FXS subjects' EEG data. Numbers indicate TDC and
559 FXS experimental IDs.
560
561 **Supplemental Figure 4. Elevated m^6A levels associated with increased m^6A writer**
562 **expression in *Fmr1* knockout mice. a**. Increased m^6A levels in *Fmr1* knockout mice compared
563 to wild type (WT) mice. Shown are dot blot assays of polyA$^+$ RNA m^6A levels and quantification
564 of m^6A intensity in *Fmr1* knockout neurons relative to WT, normalized to methylene blue (n = 4
565 samples; ***$p < 0.001$; two-tailed t-test). **b**. Transcriptional expression analysis revealing no
566 significant change of METTL3, METTL14, and WTAP transcripts from RNA sequencing between
567 WT and *Fmr1* knockout mice. Values represent mean ± s.e.m. (n = 2 wild type and 2 *Fmr1*
568 knockout mice; n.s. denotes non-significance; two-tailed t-test). **c-d**. Western blot analysis and
569 quantification of FMRP, METTL3, and WTAP protein levels. Values represent mean ± s.e.m. (n =
570 4 samples; ***$p < 0.001$; two-tailed t-test).
571

572 **Supplemental Figure 5. Transcriptome-wide m^{6}A dysregulation in postmortem brain**
573 **tissues from FXS subjects. a-c**. Transcriptome-wide m^{6}A profiling in postmortem brain tissue
574 (Brodmann area 44) derived from FXS subjects and healthy controls. **a**. Metagene plot showing
575 m^{6}A peak distribution across human chromosomes. **b**. Sequence logo depicting the top
576 enriched motif in m^{6}A peaks (p value = 10^{-4}). **c**. Distribution of m^{6}A methylation across
577 transcripts, with each transcript divided into 5′ UTR, CDS, and 3′ UTR. **d**. Volcano plot
578 displaying MeRIP-seq data of differentially methylated m^{6}A peaks between FXS and control
579 groups (n = 3 healthy controls and 3 FXS samples; adjusted p-value < 0.01; blue and red dots
580 indicate significant hypo- and hyper-methylated sites, respectively). **e-f**. Histogram illustrating
581 the distribution of hypo- and hyper-methylated sites per gene (**e**) and per chromosome length
582 (**f**), with blue and red boxes indicating hypo- and hyper-methylated sites, respectively. **g**. Gene
583 Ontology (GO) term analysis of differentially methylated genes (DMGs) between FXS subjects
584 and controls, showing top 15 enrichment terms for cellular component (CC) and biological
585 process (BP). The color represents the adjusted P-value, and the size of the shape represents
586 the gene ratio (percentage of total DMGs in the given GO term). **h-j**. Venn diagrams showing
587 the overlap between hypermethylated transcripts and FMRP target transcripts (**h**), SAFRI ASD
588 genes (**i**), and reported synapse-related genes (**j**), along with representation factors and p-
589 values. **k-l**. GO term analysis of overlapped genes between hypermethylated transcripts and
590 FMRP target transcripts (**k**) and between hypermethylated transcripts and SAFRI ASD genes
591 (**l**).
592
593 **Supplemental Figure 6. Correlation of hypermethylation with gene downregulation in**
594 **postmortem brain tissues from FXS subjects. a**. Venn diagram, drawn to scale, shows the
595 overlap between differentially expressed genes (DEGs) in FXS iPSCs-derived neurons and
596 controls, and FMRP target transcripts, with representation factor and P-value. **b**. Gene Ontology
597 (GO) term analysis of overlapped genes between hypermethylated transcripts and FMRP target
598 transcripts reveals the top 15 enriched terms for cellular component (CC) and biological process
599 (BP). The color represents the adjusted p-value, and the size represents the gene ratio,
600 indicating the percentage of total DMGs within each GO term. **c**. Venn diagram shows the
601 overlap between DEGs and reported synaptic genes, with representation factor and P-value. **d**.
602 Volcano plot illustrating differential gene expression analysis in postmortem brain tissue
603 (Brodmann area 44) from FXS subjects versus healthy controls (n = 3 healthy controls and 3
604 FXS samples; fold change > 1.4, p-value < 0.05; blue and red dots represent significantly down-
605 and up-regulated genes, respectively). **e-f**. Venn diagrams show the overlap between DEGs

606 from postmortem tissues and FMRP target transcripts (**e**) and SAFRI ASD genes (**f**), along with
607 representation factors and P-values. **g-h**. GO term analysis of overlapped genes between DEGs
608 and FMRP target transcripts (**g**), as well as DEGs and SAFRI ASD genes (**h**), revealing the top
609 15 enriched terms for cellular component (CC), biological process (BP), and molecular function
610 (MF). **i**. Venn diagram illustrating the overlap between DEGs from postmortem tissues and
611 reported synaptic genes, with the representation factor and P-value. **j**. Conjoint analysis shows
612 a strong negative correlation between m^6A modifications and gene expression levels from
613 postmortem brain tissues (R = -0.33, p-value = 1.152e-53, Chi-squared test), with a notable
614 hyper-down pattern in quadrant II (hyper-methylation paired with gene downregulation, 72.9% of
615 total correlations). **k**. GO term analysis of transcripts with hyper-methylation paired with gene
616 downregulation.

617 **Methods**

618 **Participants.**

619 Seven participants with a full mutation in the *FMR1* gene were recruited through the Cincinnati
620 Fragile X Research and Treatment Center. Fragile X status was confirmed by southern blotting
621 and PCR analysis completed at Rush University. Five typically developing control (TDC) were
622 recruited through web-based fliers from the local community and had no prior diagnosis or
623 treatment for developmental or neuropsychiatric disorders. Written informed consent was
624 obtained from all participants or their legal guardians, with verbal assent provided when
625 appropriate. This study was approved by the Institutional Review Board (IRB) of Cincinnati
626 Children's Hospital Medical Center (CCHMC) and was conducted in accordance with all
627 relevant guidelines and regulations, including the Declaration of Helsinki.

628 Deviation intelligence quotient (IQ) scores, including full-scale IQ (FSIQ), non-verbal IQ
629 (NVIQ), and verbal IQ (VIQ), were assessed using the Stanford-Binet Intelligence Scales, 5th
630 Edition, with adjustments made to account for floor effects commonly seen in individuals with
631 developmental disabilities [62].

632 Blood samples were collected from seven FXS and one TDC participants for various
633 analyses: one set was used for peripheral blood mononuclear cells (PBMCs) isolation and FXS
634 induced pluripotent stem cells (iPSCs) generation, another for FMRP quantification using an
635 optimized Luminex assay as described by Boggs *et al.* [63], and a third for *FMR1* mRNA detection
636 via a sensitive RT-qPCR assay as previously described [64].

637

638 **Human postmortem brain tissue.**

639 Frozen human postmortem brain tissues (Brodmann area 44; Table 2), including samples from
640 three FXS patients (named hFXS-1, hFXS-2, and hFXS-3) and three age-matched control
641 subjects (named hUHC-1, hUHC-2, and hUHC-3), were obtained from the National Institutes of
642 Health (NIH) Neurobiobank, specifically the University of Maryland Brain and Tissue bank, and
643 the Brain Tissue Donation Program at the University of Pittsburgh.

644

645 **Generation and culture of patient iPSC lines.**

646 Whole blood samples were collected from seven male FXS and one TDC participate. PBMCs
647 were isolated using SepMate™-50 tubes (StemCell Technologies) with Lymphoprep™ Density
648 Gradient Medium (StemCell Technologies) through density-gradient centrifugation. A total of
649 500,000 PBMCs were seeded in 24-well plates and cultured in PBMC medium [StemPro®-34
650 SFM medium (ThermoFisher) supplemented with SCF (100ng/mL; Peprotech), FLT-3

651 (100ng/mL; Peprotech), IL-3 (20ng/mL; Peprotech), and IL-6 (20ng/mL; Peprotech)] for
652 four days. PBMCs were then transduced using the Cytotune™-iPS 2.0 Sendai Reprogramming
653 Kit (ThermoFisher) at the appropriate MOI, following the manufacturer's instructions, and
654 incubated overnight. The next day, the CytoTune™ 2.0 Sendai viruses were removed, and the
655 transduced PBMCs were cultured in PBMC medium for two additional days. The cells were
656 subsequently seeded on vitronectin (ThermoFisher)-coated plates in complete StemPro®-34
657 SFM medium without cytokines for four days. After this, the medium was switched to Essential
658 8™ Flex medium (ThermoFisher). Once iPSC-like colonies emerged, they were manually
659 picked and cultured in Essential 8™ Flex medium. These FXS iPSCs were labeled FXS-1, FXS-
660 2, FXS-3, FXS-4, FXS-5, FXS-6, FXS-7, separately. The TDC control iPSC was labeled
661 unaffected healthy control (UHC)-5. UHC fibroblast samples derived from five age-matched
662 male subjects were obtained from the Coriell Institute (GM00409, GM07753, GM09503,
663 GM23815, GM23976). These fibroblasts were reprogrammed into iPSCs as previously
664 described in our earlier publication [65]. Briefly, fibroblasts were transduced overnight with
665 Cytotune™-iPS 2.0 Sendai reprogramming vectors, with the medium being changed daily. After
666 seven days, the cells were transferred into vitronectin-coated plates with Essential 8™ Flex
667 medium. iPSC colonies were identified, manually picked, and expanded approximately 18 days
668 later. These control iPSCs were named UHC-1, UHC-2, UHC-3, UHC-4, UHC-6, separately.
669 Another control iPSC line, C3, previously published[66] and generously provided by Dr. Hongjun
670 Song and Guo-li Ming's labs, was renamed UHC-7 for this study.
671 All iPSCs were expanded on vitronectin-coated plates in Essential 8™ Flex medium and
672 passaged with ReleSR™ (StemCell Technologies) upon reaching 70-80% confluence using a
673 1:6 split ratio. iPSCs were cryopreserved in stem cell freezing medium [American Type Culture
674 Collection (ATCC)]. 10 μM Y27632 (Peprotech) was added during both passaging and thawing.
675 All iPSCs generated in this project have been carefully characterized in terms of their karyotype,
676 pluripotency, and expression of stemness markers.
677
678 **CGG sizing.**
679 Genomic DNA was extracted from iPSCs using the Quick-DNA Miniprep Kit (Zymo Research).
680 The CGG repeat size in the *FMR1* gene was determined by repeat-primed PCR (RP-PCR)
681 using primers flanking the CGG-repeat region of the 5' UTR in *FMR1*, as per the manufacturer's
682 instructions (AmplideX ® PCR/CE *FMR1* Kit, Asuragen). Briefly, 2 μl of purified genomic DNA
683 (40 ng/μl) was added to a master mix containing 11.45 μl GC-Rich Amp Buffer, 0.5 μl *FMR1* F, R
684 FAM-Primers, 0.5 μl *FMR1* CGG Primer, 0.5 μl diluent, and 0.05 μl GC-Rich Polymerase Mix.
685 The PCR protocol included: initial denaturation at 95 °C for 5 min, followed by 10 cycles of 97

686 °C for 35 s, 62 °C for 35 s, and 68 °C for 4 min. This was followed by 20 cycles of 97°C for 35
687 seconds, 62°C for 35 seconds, and 68°C for 4 minutes, with an additional 20-second increment
688 per cycle. The final extension was carried out at 72°C for 10 minutes. The PCR products were
689 then mixed with Hi-Di Formamide and the ROX 1000 Size Ladder. After denaturation at 95 °C
690 for 2 min and cooling to 4°C for 5 minutes, the amplicons were separated via capillary
691 electrophoresis (CE) using an ABI 3500 Genetic Analyzer with POP-7 polymer (Applied
692 Biosystems). The CGG repeat length was calculated based on the fragment size in base pairs
693 using the *FMR1* Analysis Macro (v2.1.2; Asuragen) with size and mobility conversion factors.
694
695 **Differentiation of cortical glutamatergic neurons from iPSCs**
696 Cortical glutamatergic neurons were generated from iPSCs as previously described[67, 68], with
697 some modifications as described here. Briefly, iPSCs were dissociated into single cells with
698 StemPro™ Accutase™ Cell Dissociation Reagent (ThermoFisher) and seeded at a density of
699 2,500,000 cells per well on Matrigel-coated (human embryonic stem cell-qualified matrix,
700 Corning) six-well plates in Essential 8™ Flex medium with Y27632. From day 1 to day 3, the
701 medium was switched to Essential 6™ medium (ThermoFisher) supplemented with LDN193189
702 (500 nM, Peprotech), SB431542 (10 μM, Cayman Chemical), and XAV939 (5 μM, Selleckchem)
703 (referred to as E6-LSBX medium). From day 4 to day 8, cells were maintained in E6-LSB
704 medium (without XAV939). Beginning on day 9, the medium was switched to a house-made N2
705 medium [DMEM/F12 medium with 2-mercaptoethanol (1X; ThermoFisher), sodium bicarbonate
706 (2 mg/mL; Sigma), D-(+)-Glucose (1.56 mg/mL; Sigma), progesterone (6.4 mg/mL; Sigma), N2
707 Supplement-B (0.5X; StemCell Technologies)], supplemented with B27™ (1X; ThermoFisher)
708 and FGF-8b (50ng/mL; R&D Systems) until day 21. At this stage, neuronal progenitor cells
709 (NPCs) were either cryopreserved in stem cell freezing medium or dissociated with Accutase™
710 and plated onto Poly-L-ornithine (PO, 15 μg/mL; Sigma)/Laminin (2 μg/mL; R&D
711 Systems)/Fibronectin (1 μg/mL; R&D Systems)-coated plates or coverslips. Cells were then
712 cultured in neuron medium [Neurobasal® medium (ThermoFisher) with B27™ supplement (1X),
713 BDNF (20 ng/mL; Peprotech), GDNF (20 ng/mL; Peprotech), Ascorbic Acid (AA, 0.2 mM;
714 Sigma), cAMP (100 μM; Sigma), GlutaMAX™ (1X; ThermoFisher), and MEM Non-Essential
715 Amino Acids (NEAA, 1X; ThermoFisher)] with the addition of DAPT (10 μM; Cayman Chemical).
716 Half of the neuron medium was replaced twice a week for a total of six weeks.
717
718 **Isolation of primary mouse astrocytes and co-culture with iPSC-derived cortical neurons.**

719 Primary mouse astrocytes were isolated as previously described [69], with minor modifications.
720 Brains from P0 C57BL/6J mice were dissected, and the meninges were removed. The
721 meninges-free cerebral cortices were minced into small pieces and digested with trypsin
722 (ThermoFisher) and DNase I (Sigma). The resulting cell suspension was plated onto 0.01%
723 Poly-L-Lysine (PLL; Sigma)-coated flasks in Dulbecco's Modified Eagle Medium (DMEM,
724 ThermoFisher) supplemented with 10% fetal bovine serum (FBS) (ThermoFisher). and 2%
725 penicillin/streptomycin. From day 2 to day 8, primary astrocytes were separated from
726 oligodendrocyte progenitor cells, microglia and neurons by tapping the flask and washing with
727 PBS. Primary astrocytes were cryopreserved around day 8.
728 Before co-culturing with cryopreserved iPSC-derived NPCs, primary mouse astrocytes
729 were thawed, expanded and seeded on coverslips in 24-well plates. Once the astrocyte
730 monolayer reached 80-90% confluence, cryopreserved iPSC-derived NPCs were thawed,
731 seeded directly onto the astrocytes, and differentiated in neuron medium [Neurobasal® medium
732 supplemented with B27™, BDNF, GDNF, AA, cAMP, GlutaMAX™, and NEAA] containing DAPT.
733 Half of the neuron medium was replaced twice weekly. After 6 weeks of culture, whole-cell patch
734 clamp recordings and immunocytochemistry were performed. For treatment, cultures were
735 exposed to either DMSO (0.1%; Sigma) or 10 μM STM2457 (Cayman Chemical) for 2 weeks,
736 from week 4 to week 6.
737
738 **Western blot analysis.**
739 Ten-week-old wild-type (WT) and *Fmr1*-knockout (*Fmr1*-KO) male mice, kindly provided by Prof.
740 Christina Gross, were used for protein extraction from fresh cortical tissues. Additionally, protein
741 was extracted from six-week-old iPSC-derived cortical neurons using ice-cold RIPA buffer
742 (Sigma), supplemented with cOmplete Protease Inhibitor Cocktail (Roche) and PhosSTOP™
743 (Roche). Lysates were sonicated and incubated on ice, followed by centrifugation at 4°C.
744 Protein concentrations were determined using the Pierce™ BCA Protein Assay Kit
745 (ThermoFisher). Equal amounts of protein lysates were denatured in SDS-polyacrylamide gel
746 electrophoresis (PAGE) Sample Loading Buffer (G-Biosciences), separated on 4-12% Bolt Bis-
747 Tris Plus Protein Gels (ThermoFisher), and transferred to polyvinylidene fluoride (PVDF)
748 membranes (Millipore) using the XCell SureLock™ Mini-Cell system (ThermoFisher). The
749 membranes were blocked for 1 hour at room temperature (RT) with 5% non-fat milk in Tris-
750 buffered saline containing Tween-20 (TBST) (blocking buffer), followed by overnight incubation
751 at 4°C with the following primary antibodies diluted in blocking buffer: rabbit polyclonal anti-
752 FMRP (1:1000; Abcam), rabbit monoclonal Synapsin II (1:1000; Abcam), mouse monoclonal

753 SV2 (1:1000; Santa Cruz Biotechnology), rabbit monoclonal METTL3 (1:500;
754 MedChemExpress), rabbit polyclonal METTL14 (1:1000; Sigma), rabbit monoclonal WTAP
755 (1:500; Cell Signaling Technology), and mouse monoclonal GAPDH (1:5000; Santa Cruz
756 Biotechnology). After 3 washes with TBST, the membranes were incubated for 1 hour at RT with
757 horseradish peroxidase (HRP)-coupled secondary antibodies: anti-rabbit IgG (1:5000;
758 ThermoFisher) or anti-mouse IgG (1:5000; ThermoFisher). The membranes were washed 3
759 times with TBST and visualized by the addition of SuperSignal™ West Pico PLUS
760 Chemiluminescent Substrate (ThermoFisher) directly on the membranes placed in the iBright™
761 FL 1500 Imaging System (ThermoFisher). Protein levels were normalized to GAPDH, and
762 quantitative analysis was performed using ImageJ software.
763
764 **Immunocytochemistry.**
765 Six-week-old iPSC-derived cortical neurons were fixed with 4% paraformaldehyde
766 (ThermoFisher) for 15 min at RT, then washed 3 times with PBS. They were permeabilized with
767 0.1% Triton™ X-100 (Sigma) and blocked in 3% donkey serum (Sigma) for 2 hours. Primary
768 antibodies, diluted in PBS containing 0.1% Triton X-100 and 3% donkey serum, were applied to
769 the cells and incubated overnight at 4°C. Following primary antibody incubation, cells were
770 treated with species-specific secondary antibodies (1:1000; Jackson ImmunoResearch
771 Laboratories) diluted in 3% donkey serum for 2 hours at RT. Cells were washed and cell nuclei
772 were stained with 4′,6-diamidino-2-phenylindole (DAPI) for 5 min. Coverslips were mounted in
773 fluoroshield mounting medium (Abcam), sealed with clear nail polish, and stored at 2-8°C until
774 imaging. The following primary antibodies were used: mouse monoclonal Nestin (1:500, Santa
775 Cruz Biotechnology), mouse monoclonal Sox2 (1:1000; Santa Cruz Biotechnology), mouse
776 monoclonal ZO1 (1:1000; Thermo Fisher Scientific), rabbit polyclonal Foxg1 (1:1000, Abcam),
777 mouse monoclonal PAX6 (1:1000; BD Biosciences), mouse monoclonal OTX2 (1:50; DSHB),
778 rabbit polyclonal doublecortin (1:1000; Cell Signaling Technology), mouse monoclonal BRN2
779 (1:50; DSHB), goat monoclonal CaMKII (1:500; Santa Cruz Biotechnology), mouse polyclonal
780 beta III tubulin (1:500; Sigma), rabbit polyclonal TBR1 (1:1000; Abcam), rat monoclonal CTIP2
781 (1:1000; Abcam), rabbit monoclonal Synapsin I (1:1000; Abcam), mouse monoclonal SV2
782 (1:1000; Santa Cruz Biotechnology).
783 Images were obtained on either a Nikon A1R inverted confocal laser scanning
784 microscope with 60x objectives or an Olympus BX51 with 20x objectives. Image analysis was
785 performed using NIS Elements version 5.42.06 software (Nikon) and Imaris version 10.2.0
786 software (Nikon). For neurite analysis, parameters including the number of segments, total

787 length, terminal points, branch points, maximum segment length, minimum segment length, and
788 mean segment length were assessed. Synaptic density (D) was determined by calculating the
789 total SV2 and SYN1 puncta per 100 μm of total dendritic length. For spine analysis, the ratio of
790 mature (stubby and mushroom-like) and immature spines (filopodia and thin-like) was
791 calculated.
792
793 **Whole-cell patch clamp recording.**
794 Whole-cell patch-clamp recordings were conducted at RT on iPSC-derived cortical neurons,
795 either untreated or treated with DMSO or STM2457 for 2 weeks, following a six-week co-culture
796 with primary mouse astrocytes, using a Multiclamp 700A patch-clamp amplifier (Molecular
797 Devices) as previously described [34]. Briefly, cortical neurons grown on coverslips were
798 visualized with a 40X air objective on an inverted Zeiss microscope, and the recording chamber
799 was constantly perfused with a bath solution consisting of 128 mM NaCl, 30 mM glucose, 25
800 mM HEPES, 5 mM KCl, 2 mM $CaCl_2$, and 1 mM $MgCl_2$ (pH 7.3; 315–325 Osm). Patch pipettes
801 were pulled from borosilicate glass (Sutter Instrument) with a resistance of 3-5 MΩ and filled
802 with an internal solution composed of 135 mM CsGluconate, 10 mM Trisphosphocreatine, 10
803 mM HEPES, 2.5 mM EGTA, 4 mM MgATP, 0.5 mM Na_2GTP, and 5 mM QX-314 (pH 7.3 with
804 CsOH; ~305 mOsm) for excitatory postsynaptic currents (EPSCs) and inhibitory postsynaptic
805 currents (IPSCs). EPSCs were recorded at a holding potential of -70 mV, while IPSCs were
806 recorded at +20 mV. The series resistance was typically between 10-30 MΩ. To isolate
807 spontaneous IPSCs, the bath solution was supplemented with 10 μM NBQX (Tocris Bioscience)
808 and 50 μM D-AP5 (Tocris Bioscience). For spontaneous EPSC recordings, 20 μM bicuculline
809 (Tocris Bioscience) was added. Drug application was achieved via a gravity-driven drug delivery
810 system (VC-6, Warner Instruments). Spontaneous IPSCs and EPSCs were recorded for 4
811 minutes (starting 2 minutes after break-in, to allow QX-314 to block sodium currents) at a
812 holding potential, sampled at 10 kHz, and filtered at 1 kHz. Spontaneous and evoked action
813 potentials were recorded using current clamp, while sodium and potassium currents were
814 measured using voltage clamp. Data acquisition was performed using pClamp 9 software
815 (Molecular Devices), and spontaneous synaptic events were analyzed with MiniAnalysis
816 software (Synaptosoft).
817
818 **Microelectrode array (MEA) and analysis.**
819 The 64-channel multielectrode array (MEA) recording system (MED64, Alpha MED Scientific)
820 features an array of 64 planar microelectrodes arranged in an 8 × 8 pattern (50 × 50 μm

electrodes with 150 μm spacing) and was used to non-invasively monitor the electrical activity of neuronal networks. Before use, the surface of the MED64 probe was coated with PO/laminin/fibronectin and a drop of iPSC-derived NPCs (500,000 cells) were directly plated on the top of the electrodes and cultured in B-27™ Electrophysiology Kit supplemented with BDNF (20 ng/ml), GDNF (20 ng/ml), AA (0.2 mM), cAMP (100 μM), GlutaMAX (1X), and NEAA (1X). DAPT was administered on day 1 to synchronize neuronal maturation, and the cultures were fed weekly. Spontaneous neuronal activity was recorded from weeks 4 to 8 post-differentiation for 5 minutes at a sampling rate of 20 kHz using Mobius software (Alpha MED Scientific). Data were filtered with a 1-1000 Hz frequency bandwidth.

A spike was detected when the recorded signal exceeded a threshold of ± 5.5 σ, where σ was the standard deviation (SD) of the baseline noise during quiescent periods. Spike clustering was performed using the Mobius software's 'Cluster Spikes' panel to distinguish and separate signals from multiple cells recorded on a single channel based on the shapes of their spikes, utilizing a modified version of the online 'Leader-Follower Clustering' algorithm. A valid cluster was defined by the following parameters: a minimum of 5 spikes ('Min # spikes') and 30% similarity ('Similarity %'). Next, burst activity and synchronized burst activity were analyzed by Mobius offline toolkit software (Alpha Med Scientific). Bursts were identified as sequences of at least three spikes with inter-spike intervals within 300 milliseconds and a duration exceeding 200 milliseconds. Burst duration and spikes per burst were analyzed and compared. Synchronized burst activity, representing burst events across 64 channels, was visualized using a 'time course of spike frequencies across 64 channels' plot, where spike frequencies were quantified as the array-wide spike detection rate (ASDR). Additionally, a raster plot was used to display the distribution of spike timing across all channels.

Moreover, MEA data were analyzed using UP state analysis, a method previously applied to *in vitro* brain slices from *Fmr1*-KO mice [70]. Spontaneous UP states were detected based on methods defined in Hays et al[70]. For each channel, data were normalized to zero by subtracting average, and rectified. Rectified data were then low pass filtered at 0.2 Hz. UP states were identified when the amplitude of the filtered signal exceeded the root mean square threshold for a minimum of 200 milliseconds. Events within 600 milliseconds of each other were grouped together into a single UP state. Median duration of up states as well as interval between up states was calculated for each channel.

EEG recording and preprocessing

854 Five minutes of resting state EEG data was collected from each participant. To facilitate
855 cooperation in FXS patients, participants watched a silent video during recording. EEG data
856 were recorded with a 128-electrode saline-based Hydrocel system (Magstim/EGI) at a sampling
857 rate of 1000 Hz.
858 EEG data were blinded, and all preprocessing was performed using EEGLAB (EEGLAB)[71].
859 The data were filtered offline using a bandpass filter from 0.5 to 120 Hz, and a notch filter at 60
860 Hz was used to remove power line noise. EEG data was visually inspected for channels or
861 periods affected by excessive artifacts from muscle, movement, and channel noise. Removed
862 channels were interpolated using spherical spline interpolation. Independent component
863 analysis (ICA) decomposition was performed using the EEGLAB pop_runica function, and
864 components were visually inspected to identify and remove those containing muscle, channel,
865 and eye movements. The data were then referenced to average.
866
867 **EEG Analysis**
868 Preprocessed EEG data were analyzed using MNE (v 1.6.1) and the FOOOF toolbox (v 1.1.0).
869 Power spectral density (PSD) was calculated at each electrode using Welch's method, with two
870 second segments and 50% overlap. For each subject, the PSD was averaged across all
871 channels excluding two outer rows of peripheral channels, to minimize the effect of remaining
872 muscle and movement artifact. The FOOOF toolbox was used to model the periodic and
873 aperiodic components of the average PSD for each subject. The model was computed using the
874 fixed aperiodic mode, with peak width limits of 1 to 12 Hz, maximum peak number set to 6, peak
875 threshold of 2 standard deviations, and no minimum peak height.
876
877
878 **m^6A dot blot assay on cortical neurons and *Fmr1*-KO mouse brain tissue.**
879 Ten-week-old WT and *Fmr1*-KO male mice were used for RNA extraction from fresh cortical
880 tissues. Additionally, total RNA was extracted from six-week-old iPSC-derived cortical neurons
881 using TRIzol reagent (ThermoFisher), followed by purification with Dynabeads mRNA
882 Purification Kit (ThermoFisher) according to the manufacturer's instructions. The extracted
883 mRNA was denatured and spotted onto Hybond N+ membrane (GE Healthcare), then cross-
884 linked using a Stratalinker UV Crosslinker 2400 (Stratagene). The membrane was blocked with
885 5% milk in PBST and probed overnight at 4°C with a rabbit m^6A antibody (1:250; Synaptic
886 Systems), followed by incubation with HRP-conjugated anti-rabbit IgG secondary antibody
887 (1:5000). Detection was carried out using SuperSignal™ West Pico PLUS Chemiluminescent

888 Substrate, and images were captured using the iBright™ FL 1500 Imaging System. To
889 determine the total RNA input, the membrane was stained with 0.04% methylene blue (Sigma)
890 in 0.5M sodium acetate (Millipore) prior to blocking. Quantification of dot intensity was
891 performed using ImageJ software.
892
893 **RIP-RT-qPCR.**
894 HEK293T cells were grown in DMEM supplemented with 10% FBS and transfected using
895 Lipofectamine 3000 (Thermo Fisher Scientific) according to the manufacturer's protocol. Cells
896 were either co-transfected with *FMRP-Flag* and *FUGW* plasmids or transfected with *mCherry-*
897 *Flag* plasmids. Post-transfection, cells were lysed using 1 mL of RIP lysis buffer (10 mM HEPES
898 pH 7.4, 200 mM NaCl, 30 mM EDTA, 0.5% Triton X-100) supplemented with protease inhibitors
899 and SUPERaseIN (1:500; ThermoFisher) at 4°C with rotation for 30 minutes. Cell lysates were
900 then cleared by centrifugation at 20,000× g at 4°C for 15 min. 10% of the supernatant was
901 saved for RNA extraction and protein extraction as input controls. The remaining supernatants
902 were incubated overnight at 4°C with ANTI-FLAG® M2 Affinity Gel (Sigma) with rotation. The
903 immunoprecipitated protein-RNA complexes were subsequently washed three times with RIP
904 wash buffer (10 mM HEPES, pH 7.4, 400 mM NaCl, 30 mM EDTA, 0.5% Triton X-100, 2X
905 protease inhibitors, and 1:1000 SUPERaseIN). Saved input and immunoprecipitated proteins
906 were eluted with sample loading buffer for SDS-PAGE, followed by western blotting using rabbit
907 polyclonal FMRP (1:1000; Abcam) and mouse monoclonal GAPDH (1:5000; Santa Cruz
908 Biotechnology). The saved input and immunoprecipitated RNA were extracted with TRIzol
909 reagent (ThermoFisher) and subjected to RT-qPCR with primers (listed in Table S1), normalizing
910 to input RNA. Reverse transcription was performed using the High-Capacity cDNA Reverse
911 Transcription Kit (ThermoFisher), and RT-qPCR was conducted using PowerUp SYBR Master
912 Mix (ThermoFisher) on a QuantStudio system.
913
914 **Polysome profiling and polysome-associated mRNA analysis.**
915 Sucrose density gradient centrifugation was employed to separate the ribosome fractions as
916 described previously [59]. Briefly, six-week-old cortical neurons were cultured with 100 µg/mL
917 cycloheximide (CHX; Sigma) supplement for 10 min at 37 °C prior to cell harvest. Cells were
918 washed in ice-cold PBS containing 100 µg/mL CHX and harvested in polysome lysis buffer (5
919 mM Tris-HCl, pH7.5, 2.5 mM MgCl2, 1.5 mM KCl, 1 mM DTT,0.5% Triton X-100, 0.5% sodium
920 deoxycholate, 100 µg/mL CHX, 40 U/ml RNaseOUT, 0.2 mg/mL heparin and protease inhibitor
921 cocktail). Cells were lysed by pipetting several times and incubation on ice for 15 min, followed

922 by centrifugation at 10,000 x g for 10 min at 4 °C. 10–50% linear sucrose gradient was
923 prepared using Biocomp Gradient Master 108 with pre-layered 10% and 50% sucrose in the
924 gradient buffer (5 mM Tris-HCl, pH7.5, 2.5 mM MgCl2,1.5 mM KCl, 2 mM DTT, 100 µg/mL CHX,
925 40 U/ml RNaseOUT, 0.1 mg/mL heparin and protease inhibitor cocktail). 300 µl supernatant of
926 cell lysate was layered on the top the sucrose gradient and centrifuged at Beckman SW41 rotor
927 in Beckman Ultra-clear tube at 4 °C, 39K rpm for 2 hrs. Gradients were fractionated while
928 monitoring absorbance at A260 with a Biocomp Piston Gradient Fractionator system according
929 to the manufacturer protocol. The areas of monosome fractions (#6-11) and heavy polysome
930 fractions (#18-25) were calculated using GraphPad Prism 6 (GraphPad Software Inc.). Total
931 RNA in each fraction was isolated using TRIzol Reagent. 200 ng of RNA in each fraction was
932 reverse transcribed to cDNA using a High-Capacity cDNA Reverse Transcription Kit. RT-qPCR
933 for target genes (*WTAP*, *METTL3* and *METTL14*) in each fraction were carried out using
934 PowerUp SYBR Master Mix. The target gene mRNA in each fraction was normalized to *GAPDH*
935 in this fraction; the abundance in the heavy polysomes was calculated by summing up fractions
936 #18-25 and compared between UHC and FXS cortical neurons.
937
938 **MeRIP-seq, MeRIP-RT-qPCR and analysis**
939 The mRNAs from total RNAs were isolated from six-week-old cortical neurons, as well as
940 postmortem brain tissues, using Dynabeads mRNA Purification Kit. Purified mRNA samples
941 were fragmented to 100-200 nt with 10X RNA Fragmentation Buffer (100 mM Tris-HCl, 100 mM
942 $ZnCl_2$ in nuclease-free H_2O). The reaction was stopped by adding 10X EDTA (0.5M). 10% of the
943 fragmented RNA was set aside as an input sample, while the remaining RNA was used for m^6A
944 immunoprecipitation. The fragmented RNA was incubated with anti-m^6A antibody (Synaptic
945 Systems) for 3 h at 4°C and then with protein G magnetic beads (ThermoFisher) at 4°C for an
946 additional 2 h to obtain immunoprecipitated RNA fragments. The m^6A-enriched RNA was
947 extracted using TRIzol. The library was prepared following the instructions for Kapa RNA
948 HyperPrep Kit (Roche). Both the input samples without IP and the m^6A IP samples were
949 subjected to 150-bp, paired-end sequencing on an Illumina NovaSeq 6000 sequencer at CD
950 Genomics.
951 For MeRIP-seq analysis, quality control of raw sequencing reads was assessed using
952 FastQC (v0.11.7). Raw reads in fastq format were then subjected to trimming, eliminating
953 adaptor sequences, reads with adaptor contaminants, and low-quality reads, using Trim Galore
954 (v0.6.6). The preprocessed reads were aligned to the human genome (GRCh38) employing
955 STAR (v2.7.9) with default settings. m^6A peaks were identified using the R package exomePeak

956 (v2.16.0) with the following parameters: “PEAK_CUTOFF_PVALUE = NA,
957 PEAK_CUTOFF_FDR = 0.05, FRAGMENT_LENGTH = 200”. The distributions of m^6A peaks
958 across the chromosomes in both UHC and FXS cortical neurons were analyzed using circos
959 (v0.69.8). Differential m^6A peak were identified using exomePeak R package under parameters:
960 “PEAK_CUTOFF_PVALUE = NA, PEAK_CUTOFF_FDR = 0.05, FRAGMENT_LENGTH=200”.
961 The output “sig_diff_peak” file was further filtered using the condition “diff.lg.fdr > 2”, generating
962 a highly significant differential m^6A peak file between FXS and control neurons (Table S2), as
963 well as between hFXS and hUHC postmortem brain tissues (Table S4). This dataset was then
964 categorized into hypermethylated and hypomethylated m^6A peaks based on the diff.log2.fc
965 values. Peaks with “diff.log2.fc” > 0 were classified as hypermethylated, while those with
966 “diff.log2.fc” < 0 were classified as hypomethylated (Table S2 and S4). Identified m^6A peaks
967 were visualized using the Integrative Genomics Viewer (IGV, v2.15.4) with bam formats. Gene
968 ontology (GO) analysis was performed using the clusterProfiler R package (v4.11.0), with
969 visualizations generated in RStudio (v3.4.3) using the ggplot2 package (v3.5.1). In the plots,
970 circle size corresponds to the percentage of genes in each ontology group, and color represents
971 the p-value for gene enrichment associated with each GO term. m^6A-RNA-related genomic
972 features were visualized using Guitar R package (v2.14.0), and de novo motif analysis was
973 performed with homer (v4.11).
974 To examine m^6A modifications on individual genes in six-week-old cortical neurons,
975 MeRIP-RT-qPCR was performed using the same procedures, except that RNAs were sheared
976 into approximately 200 nt fragments. Total RNAs were isolated from neurons untreated or
977 treated with DMSO or STM2457 for 48 hours. Primers were designed to target different m^6A
978 modification sites identified through MeRIP-seq data, including 5 sites for *APC2*, 1 site for
979 *CASKIN1,* 2 sites for *LRRC4B,* 2 sites for *NRXN2,* 1 site for *SLC8A2,* and 1 site for *SYP.* All
980 primers used for MeRIP-RT-qPCR are listed in Table S1. RT-qPCR was conducted using
981 PowerUp SYBR Master Mix on a QuantStudio system. m^6A enrichment was determined by RT-
982 qPCR analysis, calculating the percentage of a target gene in IP fraction relative to the input
983 fraction using the formula: %Input = $2^{\wedge}$ (Ct of target gene in IP - adjusted Ct of target gene in
984 input).
985
986 **Bulk RNA sequencing and analysis.**
987 Total RNAs were extracted from six-week-old cortical neurons using TRIzol reagent followed by
988 mRNAs isolation with the Dynabeads mRNA Purification Kit. Sequencing libraries were
989 prepared using NEBNext Ultra RNA Library Prep kit (New England Biolabs) for Illumina

following manufacturer's protocol. Briefly, mRNAs were fragmented and reverse-transcribed to synthesize double-stranded cDNAs. After end repair and 3' adenylation, Illumina-compatible adapters for multiplexing were ligated to the ends of the double-stranded cDNA fragments. The ligation products were then amplified and purified to generate sequencing libraries. Sequencing was performed on an Illumina NovaSeq 6000 platform with 150 bp paired end reads at Novogene Bioinformatics Technology Co., Ltd (Beijing, China).

For RNA-seq analysis, similar to the MeRIP-seq workflow, sequence reads obtained from RNA-seq were initially processed and aligned to the human genome (GRCh38) employing STAR (v2.7.9) with default settings. Gene counts were obtained using FeatureCounts (v2.0.3). Differential expression analysis was performed using the R package DESeq2, with a p value cutoff of 0.05 and a fold change threshold of log2 (fold change) > ±1. The differentially expressed genes (DEGs) between FXS and UHC cortical neurons were presented in Table S3. GO enrichment analysis was performed using the clusterProfiler R package (v4.11.0) for functional annotation.

DEGs between hFXS and hUHC postmortem brain tissues were identified using the MeRIP-seq input sequencing data, following the aforementioned RNA-seq data analysis pipeline. These DEGs are presented in Table S5. Additionally, published MeRIP-seq data for two *Fmr1*-KO and two WT mice (GSE107434) were downloaded from the NCBI Gene Expression Omnibus (GEO) database (https://www.ncbi.nlm.nih.gov/geo/query/acc.cgi?acc=GSE107434) and re-analyzed using the MeRIP-seq input sequencing data, following the aforementioned RNA-seq analysis pipeline for DEGs. The DEGs between *Fmr1*-KO and WT mice brain cortex tissues are presented in Table S6.

RNA stability assay

For six-week-old cortical neurons, treated or untreated with DMSO or STM2457 for 48 hours, transcription was inhibited by adding 5 μg/ml of actinomycin D (Cayman Chemical). Cells were harvested at 0-, 2-, and 6-hours post-actinomycin D treatment, washed with PBS, and lysed in TRIzol. Reverse transcription was performed using the High-Capacity cDNA Reverse Transcription Kit. RT-qPCR for target genes (*SYT7*, *LRRC4B*) was then conducted using PowerUp SYBR Master Mix on a QuantStudio system. Gene expression levels were normalized to *GAPDH*. All primers used are listed in Table S1.

Data collection and statistics.

All experiments were performed in triplicate or more, with data collected from parallel cultures. Detailed sample sizes and descriptions of the sample collection are provided in each figure legend. Quantitative data are presented as mean ± S.E.M. The specific statistical tests used for comparisons are indicated in the corresponding figure legends. A significance threshold of $p < 0.05$ was applied. Statistical analyses, including two-tailed t-tests, Chi-square tests, one-way ANOVA with multiple comparisons, and two-way ANOVA with multiple comparisons, were conducted using RStudio (v3.4.3) and GraphPad Prism 6.

Data and code availability.

The RNA-seq data generated in this study has been deposited in the GEO database under accession number GSE278697. The m^6A-seq data has also been submitted to GEO with accession number GSE278698. Additional data, including differential expression genes (DEGs), m^6A peak calling and annotation, FMRP targets, SAFRI ASD genes, synaptic genes, and overlap analyses, are provided in the Supplementary Materials (Tables S2-S6). All other relevant data is available upon request from the corresponding author. Commands used to run software such as STAR, exomePeak, Homer, and Guitar are included in the respective software manuals, which are publicly accessible online. R scripts used for bioinformatics analyses are available upon request.

1041 **Reference**

1042 1. Bear, M.F., Huber, K.M. & Warren, S.T. The mGluR theory of fragile X mental retardation.
1043 *Trends Neurosci* **27**, 370-377 (2004).
1044 2. Dolen, G. & Bear, M.F. Role for metabotropic glutamate receptor 5 (mGluR5) in the
1045 pathogenesis of fragile X syndrome. *J Physiol* **586**, 1503-1508 (2008).
1046 3. Nelson, S.B. & Valakh, V. Excitatory/Inhibitory Balance and Circuit Homeostasis in Autism
1047 Spectrum Disorders. *Neuron* **87**, 684-698 (2015).
1048 4. Gibson, J.R., Bartley, A.F., Hays, S.A. & Huber, K.M. Imbalance of neocortical excitation
1049 and inhibition and altered UP states reflect network hyperexcitability in the mouse
1050 model of fragile X syndrome. *J Neurophysiol* **100**, 2615-2626 (2008).
1051 5. Gao, R. & Penzes, P. Common mechanisms of excitatory and inhibitory imbalance in
1052 schizophrenia and autism spectrum disorders. *Curr Mol Med* **15**, 146-167 (2015).
1053 6. Contractor, A., Klyachko, V.A. & Portera-Cailliau, C. Altered Neuronal and Circuit
1054 Excitability in Fragile X Syndrome. *Neuron* **87**, 699-715 (2015).
1055 7. Berry-Kravis, E.M. *et al.* Drug development for neurodevelopmental disorders: lessons
1056 learned from fragile X syndrome. *Nat Rev Drug Discov* **17**, 280-299 (2018).
1057 8. Erickson, C.A. *et al.* Fragile X targeted pharmacotherapy: lessons learned and future
1058 directions. *J Neurodev Disord* **9**, 7 (2017).
1059 9. Liu, X.S. *et al.* Rescue of Fragile X Syndrome Neurons by DNA Methylation Editing of the
1060 FMR1 Gene. *Cell* **172**, 979-992 e976 (2018).
1061 10. Achuta, V.S. *et al.* Functional changes of AMPA responses in human induced pluripotent
1062 stem cell-derived neural progenitors in fragile X syndrome. *Sci Signal* **11** (2018).
1063 11. Zhang, Z. *et al.* The fragile X mutation impairs homeostatic plasticity in human neurons
1064 by blocking synaptic retinoic acid signaling. *Sci Transl Med* **10** (2018).
1065 12. Raj, N. *et al.* Cell-type-specific profiling of human cellular models of fragile X syndrome
1066 reveal PI3K-dependent defects in translation and neurogenesis. *Cell Rep* **35**, 108991
1067 (2021).
1068 13. Kang, Y. *et al.* A human forebrain organoid model of fragile X syndrome exhibits altered
1069 neurogenesis and highlights new treatment strategies. *Nat Neurosci* **24**, 1377-1391
1070 (2021).
1071 14. Sharma, S.D. *et al.* Astrocytes mediate cell non-autonomous correction of aberrant firing
1072 in human FXS neurons. *Cell Rep* **42**, 112344 (2023).
1073 15. Geula, S. *et al.* Stem cells. m6A mRNA methylation facilitates resolution of naive
1074 pluripotency toward differentiation. *Science* **347**, 1002-1006 (2015).
1075 16. Liu, J. *et al.* A METTL3-METTL14 complex mediates mammalian nuclear RNA N6-
1076 adenosine methylation. *Nat Chem Biol* **10**, 93-95 (2014).
1077 17. Ping, X.L. *et al.* Mammalian WTAP is a regulatory subunit of the RNA N6-
1078 methyladenosine methyltransferase. *Cell Res* **24**, 177-189 (2014).
1079 18. Horiuchi, K. *et al.* Identification of Wilms' tumor 1-associating protein complex and its
1080 role in alternative splicing and the cell cycle. *J Biol Chem* **288**, 33292-33302 (2013).
1081 19. Patil, D.P. *et al.* m(6)A RNA methylation promotes XIST-mediated transcriptional
1082 repression. *Nature* **537**, 369-373 (2016).

1083 20. Yang, Y., Hsu, P.J., Chen, Y.S. & Yang, Y.G. Dynamic transcriptomic m(6)A decoration:
1084 writers, erasers, readers and functions in RNA metabolism. *Cell Res* **28**, 616-624 (2018).
1085 21. Jia, G. *et al.* N6-methyladenosine in nuclear RNA is a major substrate of the obesity-
1086 associated FTO. *Nat Chem Biol* **7**, 885-887 (2011).
1087 22. Zheng, G. *et al.* ALKBH5 is a mammalian RNA demethylase that impacts RNA metabolism
1088 and mouse fertility. *Mol Cell* **49**, 18-29 (2013).
1089 23. Jiang, X. *et al.* The role of m6A modification in the biological functions and diseases.
1090 *Signal Transduct Target Ther* **6**, 74 (2021).
1091 24. He, P.C. & He, C. m(6) A RNA methylation: from mechanisms to therapeutic potential.
1092 *EMBO J* **40**, e105977 (2021).
1093 25. Yue, Y., Liu, J. & He, C. RNA N6-methyladenosine methylation in post-transcriptional gene
1094 expression regulation. *Genes Dev* **29**, 1343-1355 (2015).
1095 26. Weng, Y.L. *et al.* Epitranscriptomic m(6)A Regulation of Axon Regeneration in the Adult
1096 Mammalian Nervous System. *Neuron* **97**, 313-325 e316 (2018).
1097 27. Xu, H. *et al.* m(6)A mRNA Methylation Is Essential for Oligodendrocyte Maturation and
1098 CNS Myelination. *Neuron* **105**, 293-309 e295 (2020).
1099 28. Yoon, K.J. *et al.* Temporal Control of Mammalian Cortical Neurogenesis by m(6)A
1100 Methylation. *Cell* **171**, 877-889 e817 (2017).
1101 29. Livneh, I., Moshitch-Moshkovitz, S., Amariglio, N., Rechavi, G. & Dominissini, D. The
1102 m(6)A epitranscriptome: transcriptome plasticity in brain development and function.
1103 *Nat Rev Neurosci* **21**, 36-51 (2020).
1104 30. Shi, H. *et al.* m(6)A facilitates hippocampus-dependent learning and memory through
1105 YTHDF1. *Nature* **563**, 249-253 (2018).
1106 31. Engel, M. *et al.* The Role of m(6)A/m-RNA Methylation in Stress Response Regulation.
1107 *Neuron* **99**, 389-403 e389 (2018).
1108 32. O'Roak, B.J. *et al.* Sporadic autism exomes reveal a highly interconnected protein
1109 network of de novo mutations. *Nature* **485**, 246-250 (2012).
1110 33. Iossifov, I. *et al.* Low load for disruptive mutations in autism genes and their biased
1111 transmission. *Proc Natl Acad Sci U S A* **112**, E5600-5607 (2015).
1112 34. De Rubeis, S. *et al.* Synaptic, transcriptional and chromatin genes disrupted in autism.
1113 *Nature* **515**, 209-215 (2014).
1114 35. Zhou, X. *et al.* Integrating de novo and inherited variants in 42,607 autism cases
1115 identifies mutations in new moderate-risk genes. *Nat Genet* **54**, 1305-1319 (2022).
1116 36. Richter, J.D. & Zhao, X. The molecular biology of FMRP: new insights into fragile X
1117 syndrome. *Nat Rev Neurosci* **22**, 209-222 (2021).
1118 37. Darnell, J.C. & Klann, E. The translation of translational control by FMRP: therapeutic
1119 targets for FXS. *Nat Neurosci* **16**, 1530-1536 (2013).
1120 38. Darnell, J.C. *et al.* FMRP stalls ribosomal translocation on mRNAs linked to synaptic
1121 function and autism. *Cell* **146**, 247-261 (2011).
1122 39. Zalfa, F. *et al.* The fragile X syndrome protein FMRP associates with BC1 RNA and
1123 regulates the translation of specific mRNAs at synapses. *Cell* **112**, 317-327 (2003).
1124 40. Edupuganti, R.R. *et al.* N(6)-methyladenosine (m(6)A) recruits and repels proteins to
1125 regulate mRNA homeostasis. *Nat Struct Mol Biol* **24**, 870-878 (2017).

1126 41. Chang, M. *et al.* Region-specific RNA m(6)A methylation represents a new layer of
1127 control in the gene regulatory network in the mouse brain. *Open Biol* **7** (2017).
1128 42. Arguello, A.E., DeLiberto, A.N. & Kleiner, R.E. RNA Chemical Proteomics Reveals the N(6)-
1129 Methyladenosine (m(6)A)-Regulated Protein-RNA Interactome. *J Am Chem Soc* **139**,
1130 17249-17252 (2017).
1131 43. Edens, B.M. *et al.* FMRP Modulates Neural Differentiation through m(6)A-Dependent
1132 mRNA Nuclear Export. *Cell Rep* **28**, 845-854 e845 (2019).
1133 44. Hsu, P.J. *et al.* The RNA-binding protein FMRP facilitates the nuclear export of N(6)-
1134 methyladenosine-containing mRNAs. *J Biol Chem* **294**, 19889-19895 (2019).
1135 45. Zou, Z. *et al.* FMRP phosphorylation modulates neuronal translation through YTHDF1.
1136 *Mol Cell* **83**, 4304-4317 e4308 (2023).
1137 46. Worpenberg, L. *et al.* Ythdf is a N6-methyladenosine reader that modulates Fmr1 target
1138 mRNA selection and restricts axonal growth in Drosophila. *EMBO J* **40**, e104975 (2021).
1139 47. Zhang, F. *et al.* Fragile X mental retardation protein modulates the stability of its m6A-
1140 marked messenger RNA targets. *Hum Mol Genet* **27**, 3936-3950 (2018).
1141 48. Bagni, C. & Zukin, R.S. A Synaptic Perspective of Fragile X Syndrome and Autism
1142 Spectrum Disorders. *Neuron* **101**, 1070-1088 (2019).
1143 49. Zhang, A. *et al.* Maturation Delay of Human GABAergic Neurogenesis in Fragile X
1144 Syndrome Pluripotent Stem Cells. *Stem Cells Transl Med* **11**, 613-629 (2022).
1145 50. Das Sharma, S. *et al.* Cortical neurons derived from human pluripotent stem cells lacking
1146 FMRP display altered spontaneous firing patterns. *Mol Autism* **11**, 52 (2020).
1147 51. Pfeiffer, B.E. & Huber, K.M. The state of synapses in fragile X syndrome. *Neuroscientist*
1148 **15**, 549-567 (2009).
1149 52. Pedapati, E.V. *et al.* Neocortical localization and thalamocortical modulation of neuronal
1150 hyperexcitability contribute to Fragile X Syndrome. *Commun Biol* **5**, 442 (2022).
1151 53. Smith, E.G. *et al.* Sex differences in resting EEG power in Fragile X Syndrome. *J Psychiatr*
1152 *Res* **138**, 89-95 (2021).
1153 54. Schmitt, L.M. *et al.* Altered frontal connectivity as a mechanism for executive function
1154 deficits in fragile X syndrome. *Mol Autism* **13**, 47 (2022).
1155 55. Ethridge, L.E. *et al.* Neural synchronization deficits linked to cortical hyper-excitability
1156 and auditory hypersensitivity in fragile X syndrome. *Mol Autism* **8**, 22 (2017).
1157 56. Gerster, M. *et al.* Separating Neural Oscillations from Aperiodic 1/f Activity: Challenges
1158 and Recommendations. *Neuroinformatics* **20**, 991-1012 (2022).
1159 57. Donoghue, T. *et al.* Parameterizing neural power spectra into periodic and aperiodic
1160 components. *Nat Neurosci* **23**, 1655-1665 (2020).
1161 58. Gross, C. *et al.* Excess phosphoinositide 3-kinase subunit synthesis and activity as a novel
1162 therapeutic target in fragile X syndrome. *J Neurosci* **30**, 10624-10638 (2010).
1163 59. Cao, Y., Ye, Q., Ma, M. & She, Q.B. Enhanced bypass of PD-L1 translation reduces the
1164 therapeutic response to mTOR kinase inhibitors. *Cell Rep* **42**, 112764 (2023).
1165 60. Yankova, E. *et al.* Small-molecule inhibition of METTL3 as a strategy against myeloid
1166 leukaemia. *Nature* **593**, 597-601 (2021).
1167 61. Richter, J.D., Bassell, G.J. & Klann, E. Dysregulation and restoration of translational
1168 homeostasis in fragile X syndrome. *Nat Rev Neurosci* **16**, 595-605 (2015).

1169 62. Sansone, S.M. *et al.* Improving IQ measurement in intellectual disabilities using true
1170 deviation from population norms. *J Neurodev Disord* **6**, 16 (2014).
1171 63. Boggs, A.E. *et al.* Optimization, validation and initial clinical implications of a Luminex-
1172 based immunoassay for the quantification of Fragile X Protein from dried blood spots.
1173 *Sci Rep* **12**, 5617 (2022).
1174 64. Straub, D. *et al.* A sensitive and reproducible qRT-PCR assay detects physiological
1175 relevant trace levels of FMR1 mRNA in individuals with Fragile X syndrome. *Sci Rep* **13**,
1176 3808 (2023).
1177 65. Dao, L. *et al.* Modeling blood-brain barrier formation and cerebral cavernous
1178 malformations in human PSC-derived organoids. *Cell Stem Cell* (2024).
1179 66. Wen, Z. *et al.* Synaptic dysregulation in a human iPS cell model of mental disorders.
1180 *Nature* **515**, 414-418 (2014).
1181 67. Shi, Y., Kirwan, P. & Livesey, F.J. Directed differentiation of human pluripotent stem cells
1182 to cerebral cortex neurons and neural networks. *Nat Protoc* **7**, 1836-1846 (2012).
1183 68. Qi, Y. *et al.* Combined small-molecule inhibition accelerates the derivation of functional
1184 cortical neurons from human pluripotent stem cells. *Nat Biotechnol* **35**, 154-163 (2017).
1185 69. Guler, B.E., Krzysko, J. & Wolfrum, U. Isolation and culturing of primary mouse astrocytes
1186 for the analysis of focal adhesion dynamics. *STAR Protoc* **2**, 100954 (2021).
1187 70. Hays, S.A., Huber, K.M. & Gibson, J.R. Altered neocortical rhythmic activity states in Fmr1
1188 KO mice are due to enhanced mGluR5 signaling and involve changes in excitatory
1189 circuitry. *J Neurosci* **31**, 14223-14234 (2011).
1190 71. Delorme, A. & Makeig, S. EEGLAB: an open source toolbox for analysis of single-trial EEG
1191 dynamics including independent component analysis. *J Neurosci Methods* **134**, 9-21
1192 (2004).
1193

Acknowledgements: We would like to thank to the members of Guo Laboratory, Dr. Chuan He, as well as Drs. Aaron Zorn, James Well, and Kenneth Campbell, for their valuable comments and suggestions. We also thank Dr. Andrew Volk for providing the WTAP antibody. This study has received support from the National Institutes of Health (NIH) grants (R21NS122169 and R21MH132038), the Cincinnati Children's Hospital Medical Center (CCHMC) Trustee Grant Award, and the Local Initiative for Excellence Foundation to Dr. Ziyuan Guo. The NIH grant R01NS115507 and Department of Veteran Affairs grants I01BX002149 and IK6BX006316 to Dr. Haining Zhu are acknowledged. We would also like to express our gratitude to NIH NeuroBioBank for providing human postmortem brain tissues.

Author Contributions: Author Contributions: L.L. led and was involved in every aspect of the project. A.S. conducted whole-cell patch-clamp recording and analysis. L.D., X.C., and J.T. contributed to cell cultures and immunostaining. J.L., M.M., and E.P. conducted EEG analysis. C.M., P.T., and H.Z. performed polysome profiling analysis. G.Y., A.L., and C.W made contributions to data analysis. C.W., L.S., and C.E. provided clinical samples and data. M.C. and M.S. carried out Asuragen testing. Y.Z. contributed to MEA analysis. Y.L. and N.S. made contributions to MeRIP sequencing and RNA sequencing analysis. X.W., L.Z., and D.L. contributed to experimental design. C.G. made contributions to immunoprecipitation experiments and provide *Fmr1* knockout brains. Z.G. conceptualized and designed the project and wrote the manuscript.

Author information: MeRIP sequencing and RNA sequencing data were deposit at GEO. Correspondence and requests for materials should be address to Z.G. (Ziyuan.Guo@cchmc.org).

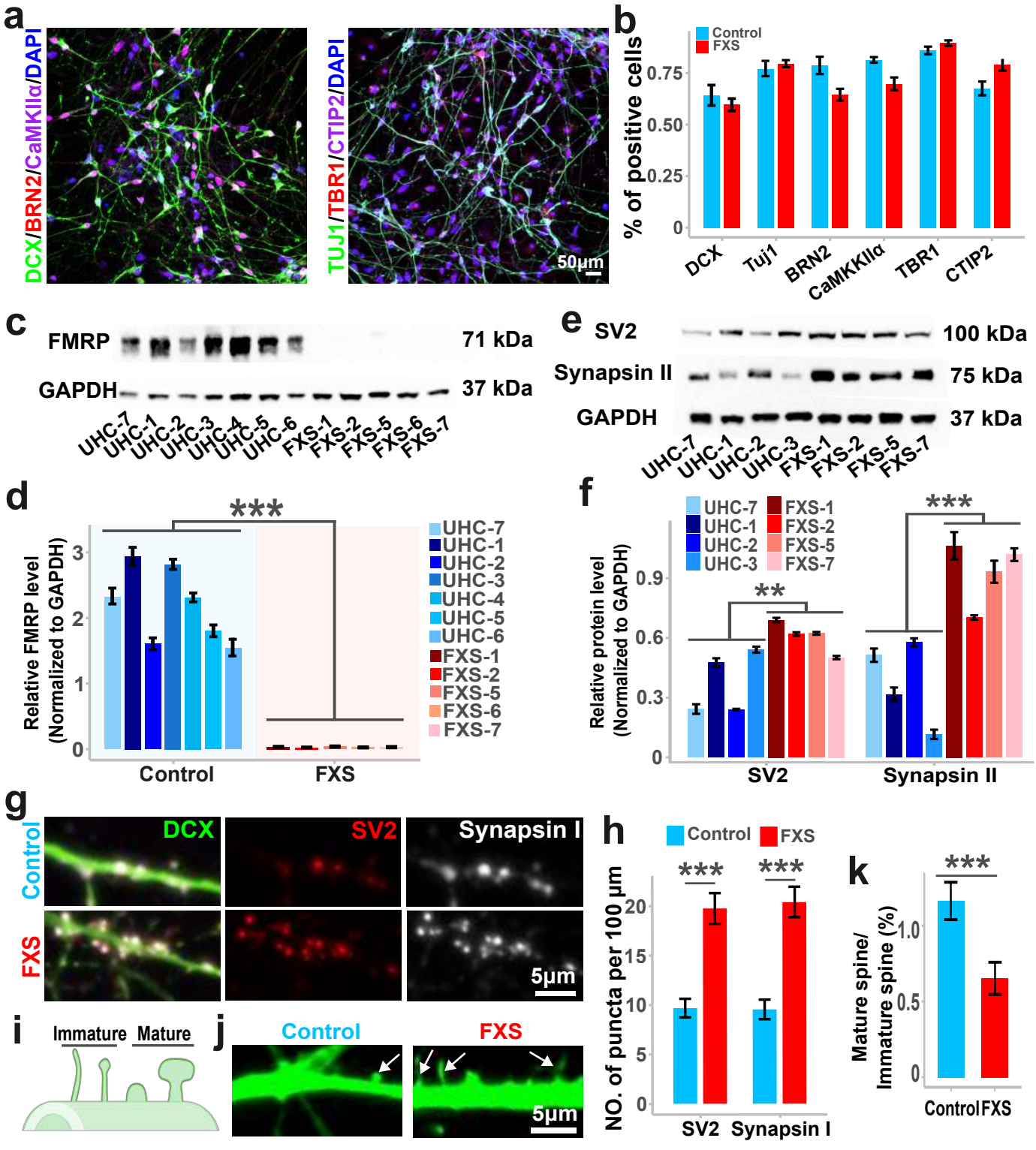

Figure 1. (Lu, et al.)

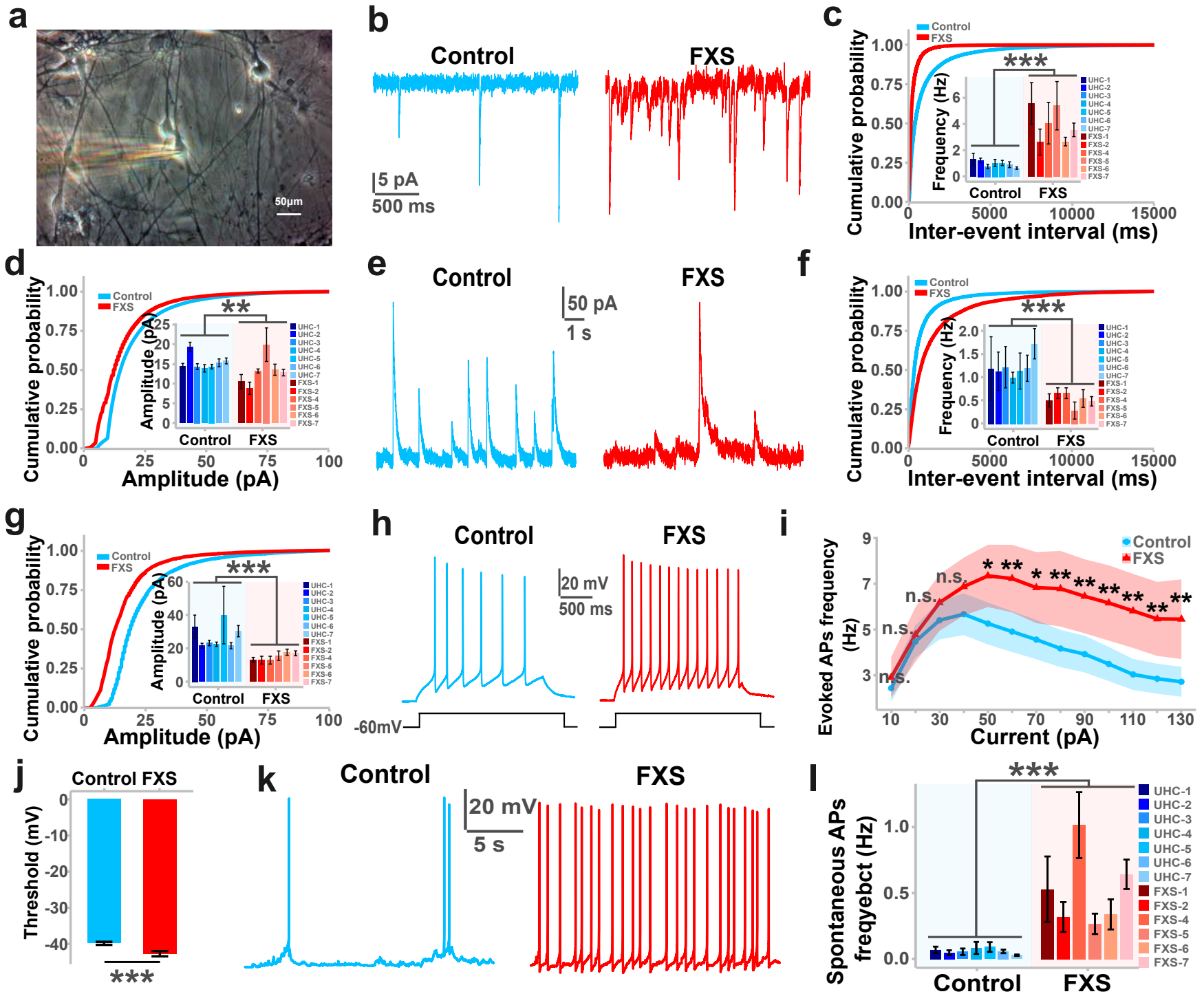

Figure 2. (Lu, et al.)

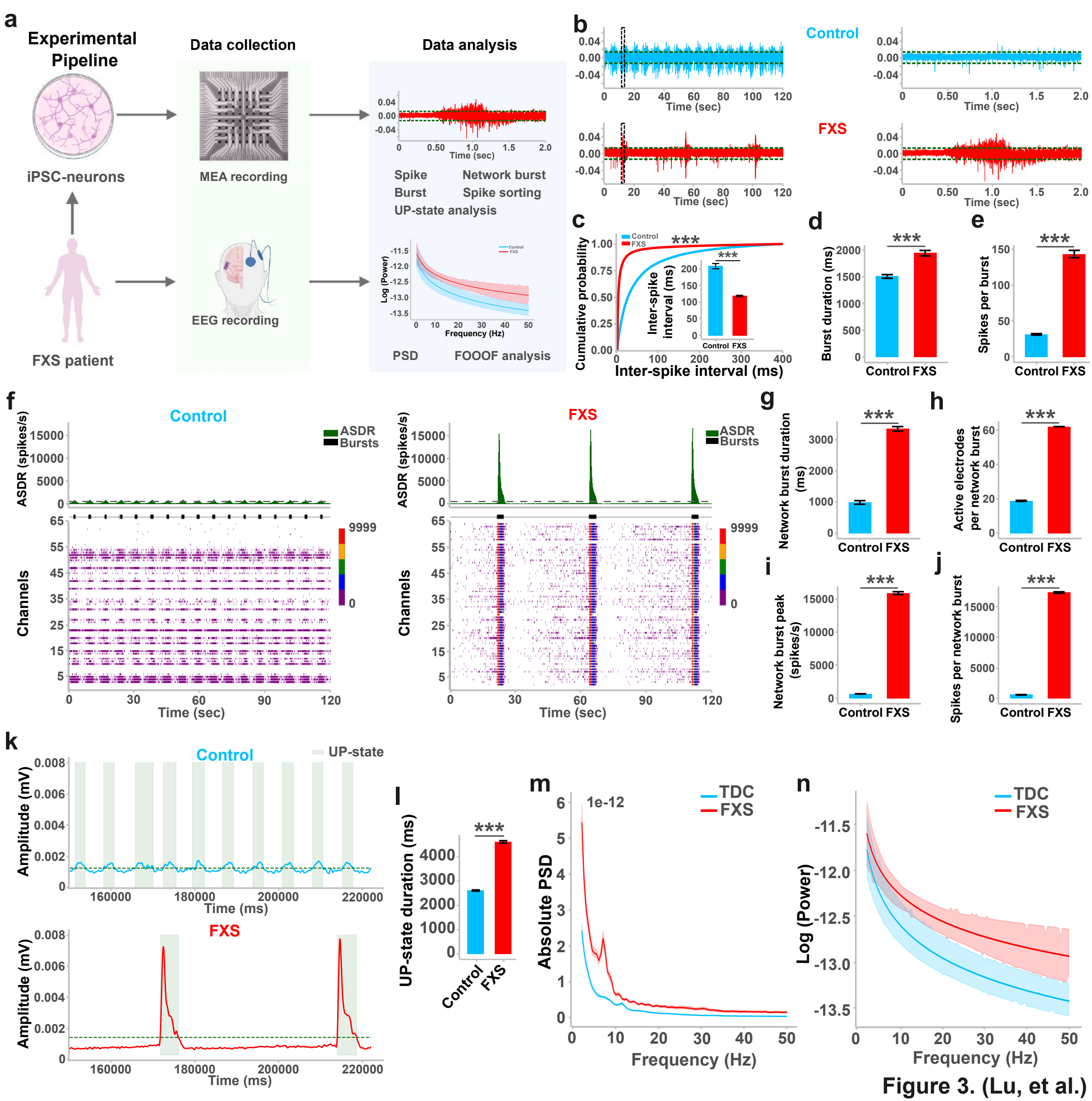

Figure 3. (Lu, et al.)

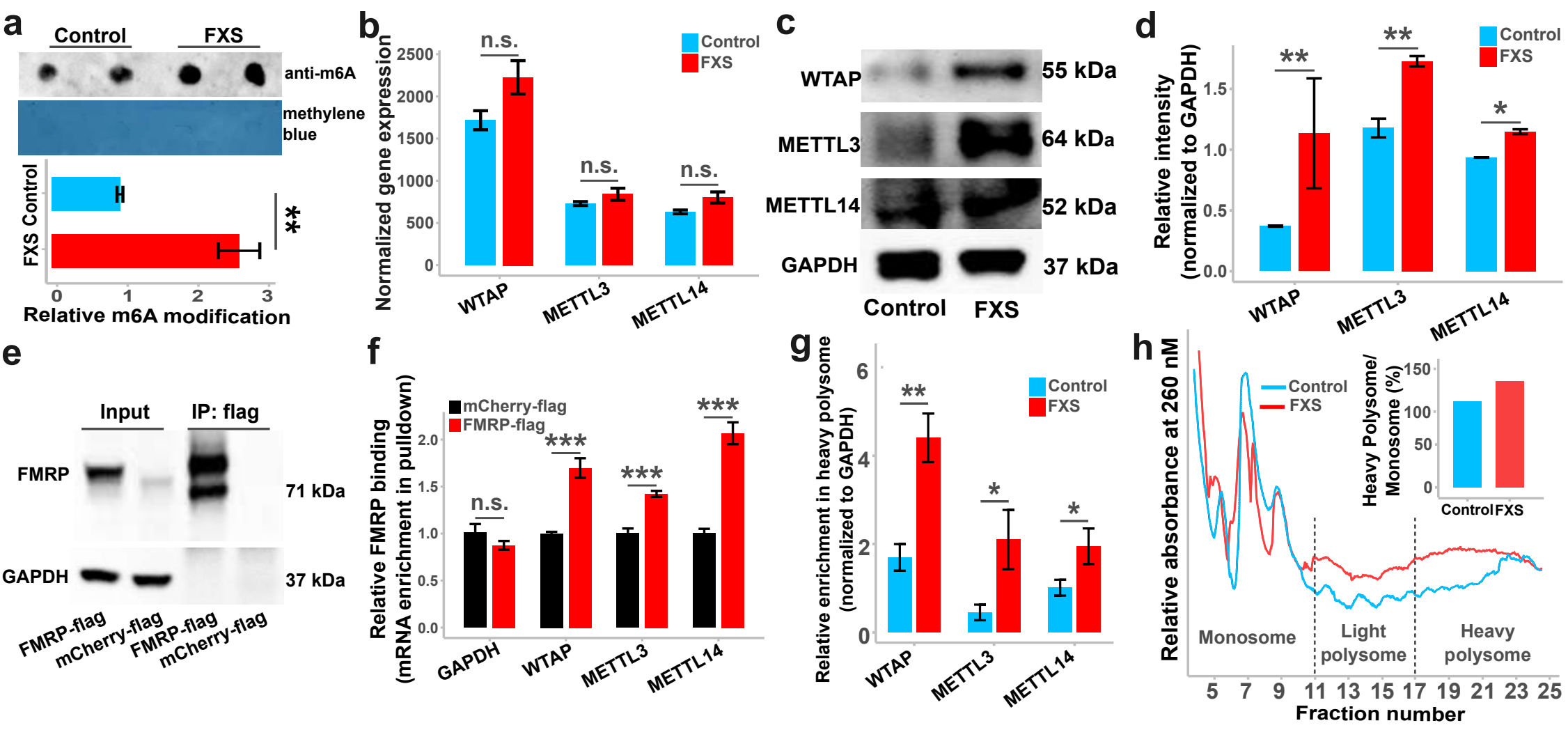

Figure 4. (Lu, et al.)

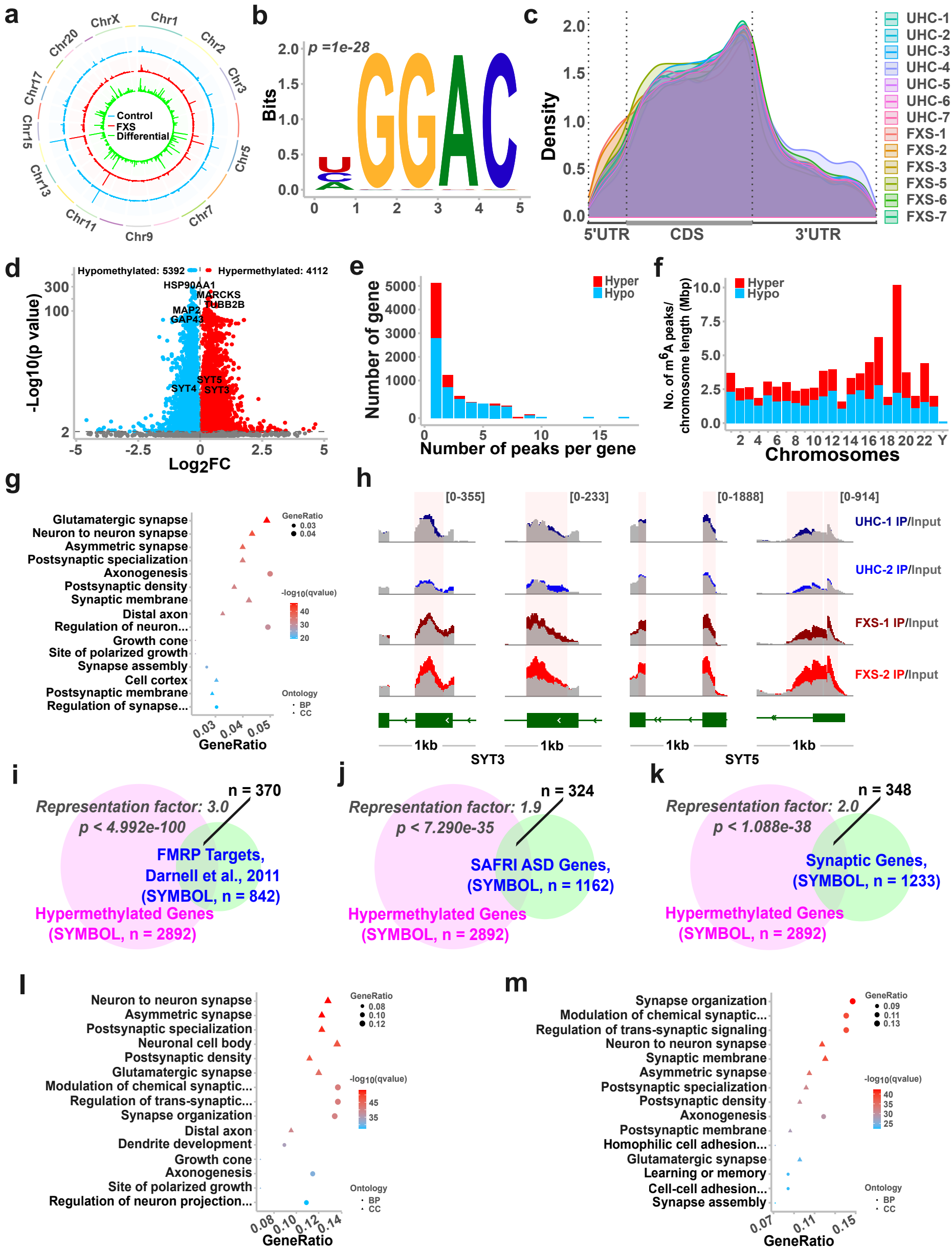

Figure 5. (Lu, et al.)

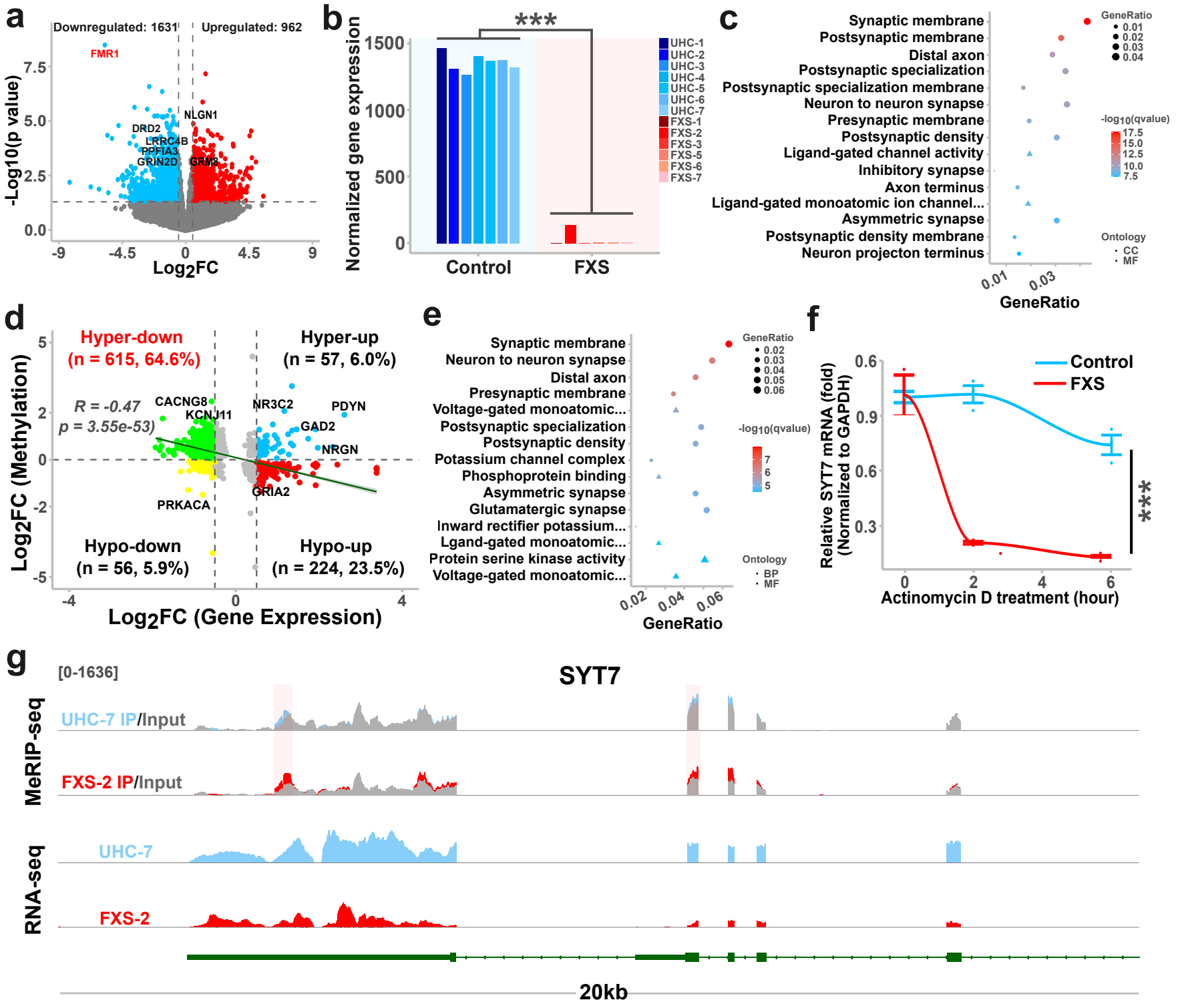

Figure 6. (Lu, et al.)

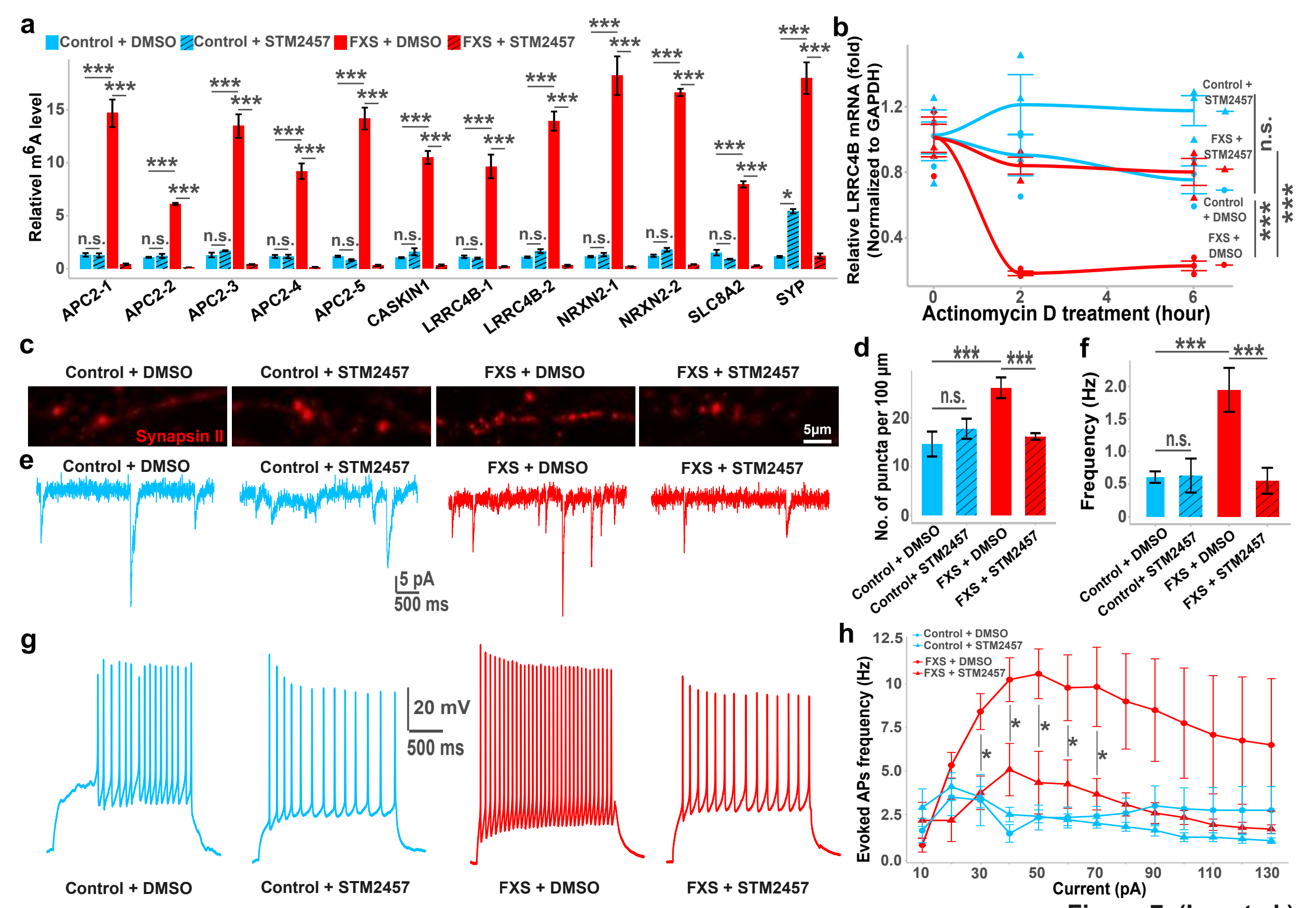

Figure 7. (Lu, et al.)

ID	Sampling Age	Gender	Diagnosis	Deviation FSIQ	Deviation NVIQ	Deviation VIQ	EEG findings	Blood Test		iPS		iPS-neurons	
								FMRP	*FMR1* mRNA	Karyotype	CGG repeats	FMRP (WB)	*FMR1* mRNA (RNA seq)
UHC-1	7	Male	N/A	-	-	-	-	-	-	Normal	30	Y	High
UHC-2	17	Male	N/A	-	-	-	-	-	-	Normal	30	Y	High
UHC-3	10	Male	N/A	-	-	-	-	-	-	Normal	30	Y	High
UHC-4	22	Male	N/A	-	-	-	-	-	-	Normal	29	Y	High
UHC-5	22	Male	N/A	-	-	-	-	-	-	Normal	29	Y	High
UHC-6	28	Male	N/A	-	-	-	-	-	-	Normal	22	Y	High
UHC-7	5	Male	N/A	-	-	-	-	-	-	Normal	29	Y	High
FXS-1	21	Male	FXS	57.35	40.37	74.32	High gamma	3.16		Normal	69, 85, 104, >200	N	Low
FXS-2	23	Male	FXS	20.25	1.65	38.85	High gamma	0	1.15E-10	Normal	164, >200, >200	N	Low
FXS-3	7	Male	FXS	33.38	29.5	37.27	High gamma	0.38	8.89E-10	Normal	>200	N	Low
FXS-4	27	Male	FXS	57.17	52.71	61.64	High gamma	9.454	1.03E-08	Normal	>200	N	Low
FXS-5	5	Male	FXS	60.4	45.97	74.83	High gamma	3.12	3.82E-09	Normal	>200	N	Low
FXS-6	10	Male	FXS							Normal	>200	N	Low
FXS-7	18	Male	FXS							Normal	>200	N	Low

Table 1. (Lu, et al)

ID	Sampling Age	Gender	Race	Diagnosis	Brain Region
hUHC-1	62	Male	White	N/A	BA44
hUHC-2	58	Male	Black or African-American	N/A	BA44
hUHC-3	44	Female	White	N/A	BA44
hFXS-1	21	Male	White	FXS	BA44
hFXS-2	85	Male	White	FXS	BA44
hFXS-3	71	Male	White	FXS	BA44

Table 2. (Lu, et al)